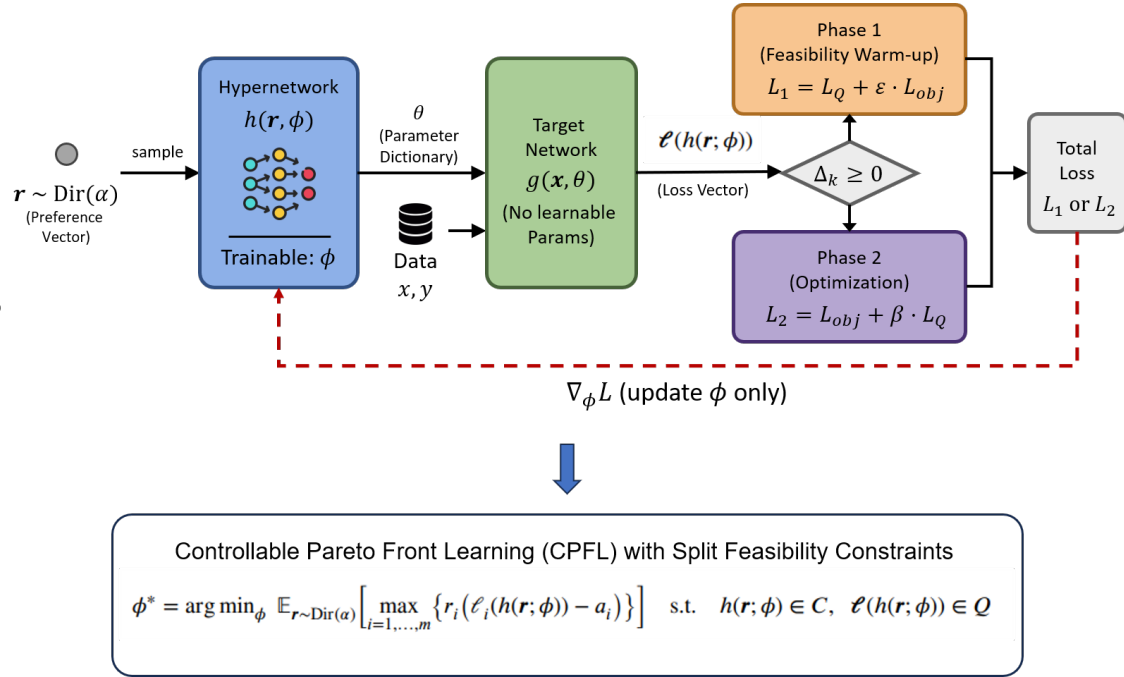


Graphical Abstract

A Two-Phase Adaptive Balanced Penalty Method for Controllable Pareto Front Learning under Split Feasibility Conditions

Nguyen Viet Hoang, Dung D. Le, Tran Ngoc Thang



Graphical Abstract: *Controllable Pareto Front Learning (CPFL) under Split Feasibility Conditions* uses a hypernetwork to map preference vectors to Pareto optimal solutions that strictly reside within a decision maker’s specified target region Q . We reformulate this constrained task as a *Bi-Level Scalarized Split Problem (BSSP)* and propose an *Adaptive Balanced Penalty* algorithm that systematically blends three gradient components—optimality, set feasibility, and image feasibility. The resulting principled penalty structure is translated into a two-phase, feasibility-first training strategy for Hyper-MLP and HyperTrans architectures, enabling reliable convergence to optimal trade-offs while consistently satisfying box and sphere constraints.

Highlights

A Two-Phase Adaptive Balanced Penalty Method for Controllable Pareto Front Learning under Split Feasibility Conditions

Nguyen Viet Hoang, Dung D. Le, Tran Ngoc Thang

- Bi-level scalarized split problem (BSSP) formulation for constrained CPFL.
- Adaptive balanced penalty (ABP) algorithm with proven full-sequence convergence.
- Two-phase feasibility-first training strategy for ABP-HyperMLP and ABP-HyperTrans.
- Expected feasible hypervolume (EFHV) metric, combining feasibility rate with feasible-subset hypervolume, shows up to $2.3\times$ improvement over baselines on three MTL datasets.

A Two-Phase Adaptive Balanced Penalty Method for Controllable Pareto Front Learning under Split Feasibility Conditions

Nguyen Viet Hoang^a, Dung D. Le^b and Tran Ngoc Thang^{a,*}

^aFaculty of Applied Mathematics and Informatics, Hanoi University of Science and Technology, Hanoi, Vietnam

^bCollege of Engineering and Computer Science, VinUniversity, Hanoi, Vietnam

ARTICLE INFO

Keywords:

Multi-objective optimization
Controllable Pareto front learning
Split feasibility problem
Hypernetwork
Transformer
Penalty method

ABSTRACT

We address the open problem of training hypernetworks for Controllable Pareto Front Learning (CPFL) under split feasibility conditions with rigorous theoretical guarantees. We reformulate the constrained Pareto problem as a *Bi-Level Scalarized Split Problem* (BSSP) and propose the *Adaptive Balanced Penalty* (ABP) algorithm, whose three gradient components—optimality, set feasibility, and image feasibility—are blended through an adaptive indicator driven by a computable lower bound. Using a novel convex surrogate technique, we prove full-sequence convergence under standard convexity and Robbins–Monro step-size assumptions. The ABP penalty structure is then translated into a two-phase, feasibility-first training strategy for Hyper-MLP and HyperTrans architectures (ABP-HyperNet). To evaluate constrained CPFL, we introduce the Expected Feasible Hypervolume (EFHV), which jointly captures solution quality and constraint satisfaction. Experiments on five multi-objective benchmarks validate the ABP solver against ground truth, while three multi-task learning datasets demonstrate that ABP-HyperNet achieves up to 2.3× higher EFHV than unconstrained baselines by raising feasibility from 36–49% to 87–100%.

1. Introduction

Multi-objective optimization (MOO) addresses problems with several conflicting objectives that must be optimized simultaneously over a shared decision space. Its applications span chemistry (Cao et al., 2019), finance (Vuong and Thang, 2023), and, notably, deep multi-task learning (MTL) (Sener and Koltun, 2018). In the MOO setting, the notion of optimality is captured by the Pareto front: the set of all non-dominated trade-off points in the objective space.

Controllable Pareto Front Learning (CPFL) trains a single model—typically a hypernetwork—that, given an arbitrary preference vector at inference time, outputs a Pareto-optimal solution corresponding to that preference. Traditional CPFL methods approximate the *entire* Pareto front (Navon et al., 2021; Lin et al., 2019), using evolutionary algorithms (Jangir et al., 2021) or Pareto set learning (Lin et al., 2022). Tuan et al. (2024a) introduced a multi-layer-perceptron-based hypernetwork (Hyper-MLP) for this task, and Tuan et al. (2024b) proposed a transformer-based variant (HyperTrans) that leverages self-attention to model pairwise trade-offs between objectives. In the multi-task learning (MTL) setting, CPFL-based approaches differ from classical gradient-balancing strategies (Sener and Koltun, 2018) in that a single hypernetwork produces task-specific weights for any given preference, enabling real-time trade-off control at inference. Crucially, all existing CPFL methods—including those of (Tuan et al., 2024a,b)—learn the *entire unconstrained* Pareto front; no mechanism is provided to restrict solutions to a decision-maker-specified region of the objective space.

The need for incorporating constraints into learning algorithms extends far beyond multi-objective optimization. In supervised learning, constraints enforce domain knowledge—such as physical laws in physics-informed neural networks (Raissi et al., 2019)—or fairness requirements across demographic groups (Agarwal et al., 2018), while in reinforcement learning, Constrained Markov Decision Processes guarantee safety during exploration (Altman, 1999; Achiam et al., 2017). More broadly, penalty and augmented Lagrangian techniques have become standard tools for embedding functional constraints into stochastic gradient training (Bertsekas, 1999; Lan and Monteiro, 2013).

In the CPFL setting specifically, the relevant constraint is an *objective-space* region Q specifying acceptable trade-off outcomes—for example, a budget constraint, a quality threshold, or a regulatory bound. This motivates *constrained*

*Corresponding author

✉ Hoang.NV227019@sis.hust.edu.vn (N.V. Hoang); dung.ld@vinuni.edu.vn (D.D. Le); thang.tranngoc@hust.edu.vn (T.N. Thang)

ORCID(s): 0009-0005-5535-3182 (N.V. Hoang)

Controllable Pareto Front Learning, which seeks to learn only the portion of the Pareto front inside Q . The mathematical framework for this type of constraint comes from *Split Feasibility Problems* (SFP), introduced by Censor and Elfving (1994), which seek a point in a closed convex set whose image under a given operator lies in another closed convex set. SFP has found applications in signal processing, image reconstruction (Byrne, 2004), and radiation therapy (Censor et al., 2005; Brooke et al., 2021); extensions to variational inequality settings were studied in (Censor et al., 2012), and the CQ algorithm of Byrne (2002) remains the most widely used solver. Tuan et al. (2024b) established the theoretical connection between SFP and Pareto front learning by formulating the Split Multi-Objective Optimization Problem (SMOP) and its outcome-space relaxation. However, the practical training procedure of (Tuan et al., 2024b) does not enforce the constraint $\mathcal{F}(x) \in Q$: the constraint region Q appears only as a heuristic regularization term in the loss function, and the resulting hypernetwork is trained to approximate the full, unconstrained Pareto front. To date, *no existing method formulates or solves constrained CPFL as a well-defined optimization problem with formal feasibility guarantees*.

In the broader context of constrained optimization, penalty-based methods have a long classical history (Bertsekas, 1999; Rockafellar, 1970), and their adaptation to the stochastic gradient setting—including convergence rate analysis under Robbins–Monro schedules—was established by Lan and Monteiro (2013). In this work, we address the above gap in two complementary steps. First, we introduce the *Bi-Level Scalarized Split Problem* (BSSP), a rigorous formulation that combines Chebyshev scalarization with split feasibility on the extended downward hull Q^+ , and we develop the *Adaptive Balanced Penalty* (ABP) algorithm (Algorithm 1) with proven full-sequence convergence. Second, we translate the penalty structure identified in this analysis—not the convergence proof itself—into a two-phase training strategy for hypernetwork-based CPFL. This strategy inherits the feasibility-first philosophy of the ABP algorithm and operates as a *convergence-theory-inspired heuristic* in the stochastic, non-convex neural network setting; its effectiveness is validated empirically in Sections 6–7. The key insight is that the three gradient components of the ABP algorithm (optimality, set feasibility, image feasibility) map directly onto the two training phases: a feasibility-first warm-up phase where the hypernetwork is driven into the constraint region Q , and a trade-off optimization phase where Chebyshev quality is maximized under an adaptive feasibility restoring force. Figure 1 provides a visual overview of this contrast.

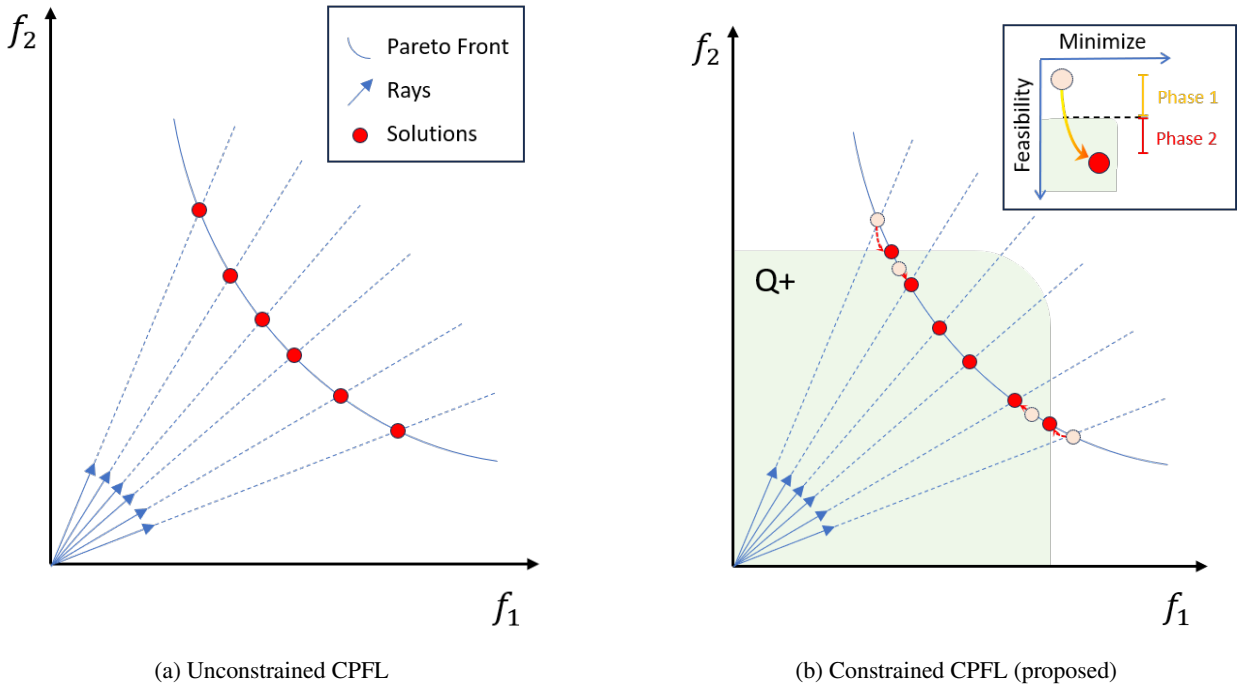


Figure 1: Conceptual overview of Controllable Pareto Front Learning. (a) Existing CPFL methods (Navon et al., 2021; Tuan et al., 2024a,b) approximate the entire unconstrained Pareto front; solutions may lie anywhere in the objective space. (b) Our BSSP two-phase training strategy restricts solutions to a decision-maker-specified region Q , systematically driving them into Q while optimizing the trade-off.

Contributions. The main contributions of this paper are threefold:

- (i) **Bi-level scalarized split problem and algorithm.** We introduce the BSSP formulation that combines Chebyshev scalarization with split feasibility on the extended downward hull Q^+ , eliminating the auxiliary variable required by the formulation of (Tuan et al., 2024b). An Adaptive Balanced Penalty algorithm is proposed that blends three gradient components—optimality, set feasibility, and image feasibility—using an adaptive indicator driven by a computable lower bound, and whose structure directly informs the two-phase training strategy.
- (ii) **Convergence guarantee.** We establish full-sequence convergence of the ABP algorithm under standard convexity and Robbins–Monro step-size assumptions, together with a zero-gap condition for which we provide verifiable sufficient conditions. The central technical device is a convex surrogate construction: at each iteration, a linearized half-space converts the non-convex image-feasibility function into a global subgradient inequality, yielding the quasi-Fejér property that drives the convergence analysis. This result supplies the theoretical justification for the two-phase training strategy described below.
- (iii) **Two-phase feasibility-first training strategy for hypernetwork-based CPFL.** Guided by the penalty structure identified in the BSSP convergence analysis, we design a practical two-phase training strategy for hypernetwork-based constrained Pareto front learning. In Phase 1 (feasibility warm-up), the hypernetwork is trained exclusively to satisfy the constraint region Q , driving all generated solutions into the feasible set before any trade-off optimization begins. In Phase 2 (trade-off optimization), the Chebyshev objective is maximized under an adaptive feasibility-restoring force that prevents constraint violations accumulated during optimality pursuit. We instantiate this strategy on two hypernetwork architectures—Hyper-MLP and HyperTrans—and evaluate it on five MOP benchmarks and three MTL datasets. The constrained configurations raise feasibility rates from 36–49% to 87–100% and achieve up to 2.3× higher EFHV than the unconstrained baselines of (Tuan et al., 2024a,b), with only a modest and controlled reduction in global hypervolume. While the convergence guarantee of Theorem 4.17 applies to the deterministic convex BSSP, the training strategy inherits the same feasibility-first philosophy and delivers consistent empirical gains across all tested settings.

Organization. The paper is organized as follows. Section 2 collects mathematical preliminaries. Section 3 develops the problem formulation from the split feasibility framework to the BSSP. Section 4 presents the Adaptive Balanced Penalty algorithm and states the main convergence results, with full proofs deferred to Appendix A. Section 5 describes the CPFL formulation and hypernetwork architectures for multi-task learning. Sections 6 and 7 present experimental results on MOP benchmarks and MTL datasets, respectively. Section 8 concludes.

2. Preliminaries

We collect definitions and tools used throughout the paper.

Definition 2.1 (Multi-objective optimization). Consider the multi-objective optimization problem

$$\min_{x \in C} \mathcal{F}(x), \quad \mathcal{F}(x) = (f_1(x), \dots, f_m(x)), \quad (\text{MOP})$$

where $C \subset \mathbb{R}^n$ is a nonempty closed convex set and each $f_i : \mathbb{R}^n \rightarrow \mathbb{R}$ is continuously differentiable. We denote the *outcome set* by $Y := \mathcal{F}(C) = \{\mathcal{F}(x) : x \in C\}$.

Definition 2.2 (Pareto optimality). A point $x^* \in C$ is *weakly Pareto optimal* for (MOP) if there is no $x \in C$ with $\mathcal{F}(x) < \mathcal{F}(x^*)$ (i.e., $f_i(x) < f_i(x^*)$ for all i). The set of weakly Pareto optimal solutions is denoted X_{WE} , and its image $Y_{WE} := \mathcal{F}(X_{WE})$ is the *weakly Pareto front*. A point $x^* \in C$ is *Pareto stationary* if $\max_{i=1, \dots, m} \nabla f_i(x^*)^\top d \geq 0$ for all $d \in \mathbb{R}^n$. When each f_i is convex, every Pareto stationary point is weakly Pareto optimal (Ehrgott, 2005).

Definition 2.3 (Chebyshev scalarization). Let $z^* = (z_1^*, \dots, z_m^*)$ be the *ideal point* defined by $z_i^* := \inf_{x \in C} f_i(x)$, assumed finite for every i . Given a preference vector $\mathbf{r} = (r_1, \dots, r_m) \in \mathbb{R}_{>0}^m$ with $\sum_{i=1}^m r_i = 1$, the *weighted Chebyshev scalarization* is

$$s(\mathcal{F}(x), \mathbf{r}) := \max_{i=1, \dots, m} \{r_i (f_i(x) - z_i^*)\}. \quad (1)$$

When each f_i is convex, $s(\mathcal{F}(\cdot), \mathbf{r})$ is convex as the pointwise maximum of convex functions. A classical result (Miettinen, 1999, Theorem 3.4.5) states that every minimizer of (1) over C is weakly Pareto optimal for (MOP).

Definition 2.4 (Extended downward hull). Let $Q \subset \mathbb{R}^m$ be a nonempty closed convex set representing a desired region in the objective space. The *extended downward hull* is

$$Q^+ := Q - \mathbb{R}_+^m = \{y - u : y \in Q, u \in \mathbb{R}_+^m\}. \quad (2)$$

The set Q^+ enlarges Q by “free disposal”: if a point belongs to Q^+ , then so does any point that is componentwise no larger. This construction plays a role analogous to the extended outcome set $Y^+ = Y + \mathbb{R}_+^m$ used in (Tuan et al., 2024b).

Lemma 2.1. *If $Q \subset \mathbb{R}^m$ is nonempty, closed and convex, then Q^+ is nonempty, closed and convex.*

PROOF. Nonemptiness and convexity follow from $Q \subset Q^+$ and the fact that Q^+ is the Minkowski sum of the convex sets Q and $-\mathbb{R}_+^m$. Closedness holds because $-\mathbb{R}_+^m$ is a polyhedral convex cone, and the Minkowski sum of a closed convex set with a polyhedral convex set is closed; see, e.g., (Rockafellar, 1970, Corollary 9.1.1), (Rockafellar and Wets, 2009, Theorem 3.12), or (Bauschke and Combettes, 2017, Theorem 6.5).

Proposition 2.2 (Free disposal). *If $z \in Q^+$ and $z' \leq z$ componentwise, then $z' \in Q^+$.*

PROOF. $z = y - u$ with $y \in Q, u \geq 0$. Then $z' = y - (u + z - z')$ with $u + z - z' \geq 0$.

We now derive an explicit formula for P_{Q^+} that is central to the algorithm.

Proposition 2.3 (Projection onto Q^+). *For every $\tilde{z} \in \mathbb{R}^m$,*

$$P_{Q^+}(\tilde{z}) = \min(\tilde{z}, y^*), \quad y^* \in \arg \min_{y \in Q} \left\| (\tilde{z} - y)_+ \right\|^2, \quad (3)$$

where \min and $(\cdot)_+$ act componentwise.

PROOF. The projection $z^* := P_{Q^+}(\tilde{z})$ exists and is unique (Lemma 2.1).

Step 1. Every $z \in Q^+$ has the form $z = y - u$ with $y \in Q, u \in \mathbb{R}_+^m$. For fixed y , the separable minimization $\min_{u \geq 0} \|y - u - \tilde{z}\|^2$ is solved componentwise by $u_j^* = \max(y_j - \tilde{z}_j, 0) = (y_j - \tilde{z}_j)_+$ for each j , giving residual $\|(\tilde{z} - y)_+\|^2$. Hence $\inf_{z \in Q^+} \|z - \tilde{z}\|^2 = \inf_{y \in Q} \|(\tilde{z} - y)_+\|^2$.

Step 2. Write $z^* = y_0 - u_0$ with $y_0 \in Q, u_0 \geq 0$. Set $\hat{u} := (y_0 - \tilde{z})_+$ and $\hat{z} := y_0 - \hat{u} \in Q^+$. By Step 1, \hat{u} is the minimizer of $\min_{u \geq 0} \|y_0 - u - \tilde{z}\|^2$, so $\|\hat{z} - \tilde{z}\|^2 \leq \|y_0 - u_0 - \tilde{z}\|^2 = \|z^* - \tilde{z}\|^2$. On the other hand, z^* is the nearest point in Q^+ to \tilde{z} , so $\|z^* - \tilde{z}\|^2 \leq \|\hat{z} - \tilde{z}\|^2$. Combining: $\|\hat{z} - \tilde{z}\|^2 = \|z^* - \tilde{z}\|^2$. Uniqueness of the projection forces $\hat{z} = z^*$. Thus $y^* := y_0$ attains the infimum in Step 1.

Step 3. $z^* = y^* - (y^* - \tilde{z})_+ = \min(y^*, \tilde{z})$.

Corollary 2.4. $\rho := \tilde{z} - P_{Q^+}(\tilde{z}) \geq 0$ componentwise for every $\tilde{z} \in \mathbb{R}^m$.

PROOF. Set $p := P_{Q^+}(\tilde{z})$. The characterization of the metric projection onto a closed convex set gives $\langle \rho, w - p \rangle \leq 0$ for all $w \in Q^+$. By Proposition 2.2, $p - te_j \in Q^+$ for every $t > 0$ and every standard basis vector e_j , so $-t\rho_j \leq 0$, whence $\rho_j \geq 0$.

Definition 2.5 (Metric projection and subdifferential). For a nonempty closed convex set $S \subset \mathbb{R}^n$, the *metric projection* $P_S(x) := \arg \min_{s \in S} \|x - s\|$ is well-defined and satisfies the variational characterization $\langle x - P_S(x), s - P_S(x) \rangle \leq 0$ for all $s \in S$. The *squared distance function* $d_S(x) := \frac{1}{2} \text{dist}^2(x, S)$ is convex and differentiable with $\nabla d_S(x) = x - P_S(x)$. For a convex function $\varphi : \mathbb{R}^n \rightarrow \mathbb{R}$, the *subdifferential* at x is $\partial\varphi(x) := \{g \in \mathbb{R}^n : \varphi(y) \geq \varphi(x) + \langle g, y - x \rangle \forall y\}$. If $\varphi = \max_i \varphi_i$ with each φ_i differentiable, then $\nabla\varphi_{i^*}(x) \in \partial\varphi(x)$ for any $i^* \in \arg \max_i \varphi_i(x)$.

3. Problem formulation

In this section, we develop the Bi-Level Scalarized Split Problem (BSSP) through a systematic chain of reformulations, following and extending the framework of (Tuan et al., 2024b).

3.1. From split feasibility to split multi-objective optimization

The *Split Feasibility Problem* (SFP), introduced by Censor and Elfving (Censor and Elfving, 1994), seeks

$$\text{Find } x^* \in C : \mathcal{F}(x^*) \in Q, \quad (\text{SFP})$$

where $C \subset \mathbb{R}^n$ and $Q \subset \mathbb{R}^m$ are nonempty closed convex sets and $\mathcal{F} : \mathbb{R}^n \rightarrow \mathbb{R}^m$ is a smooth mapping. The most widely used solver is the CQ algorithm of Byrne (2002), which iterates

$$x^{k+1} = P_C(x^k - \gamma_k J_{\mathcal{F}}(x^k)^T (\mathcal{F}(x^k) - P_Q(\mathcal{F}(x^k))))), \quad (4)$$

where P_C and P_Q denote metric projections onto C and Q , respectively, and $\gamma_k > 0$ is a step size.

The classical SFP (SFP) requires the constraint set C to be convex. However, when C is taken to be the weakly Pareto optimal solution set X_{WE} of (MOP), C is in general *non-convex*, even when \mathcal{F} is linear (Kim and Thang, 2013). This motivates the *Split Multi-Objective Optimization Problem* (SMOP) (Tuan et al., 2024b):

$$\text{Find } x^* \in X_{WE} : \mathcal{F}(x^*) \in Q. \quad (\text{SMOP})$$

Problem (SMOP) seeks a Pareto-optimal solution whose image in the objective space lies within the decision-maker's preferred region Q . To select among multiple solutions of (SMOP), Tuan et al. (2024b) considered optimizing a scalarization function over the feasible set of (SMOP):

$$\min_x S(\mathcal{F}(x)) \quad \text{s.t.} \quad x \in X_{WE}, \quad \mathcal{F}(x) \in Q, \quad (\text{SP})$$

where $S : \mathbb{R}^m \rightarrow \mathbb{R}$ is a monotonically increasing, pseudoconvex function.

Since X_{WE} is non-convex, directly solving (SP) is intractable. The *outcome-space approach* (Tuan et al., 2024b; Kim and Thang, 2013) transforms the problem using the extended outcome set $Y^+ := Y + \mathbb{R}_+^m = \{y + u : y \in Y, u \in \mathbb{R}_+^m\}$, which enjoys several favourable properties: (i) Y^+ is a closed convex set; (ii) $\partial Y^+ = Y_{WE}^+$ (the weakly efficient boundary equals the topological boundary); (iii) Y^+ is a reverse-normal set. These properties lead to the equivalent outcome-space problems:

$$\min_y S(y) \quad \text{s.t.} \quad y \in Y_{WE}^+ \cap Q, \quad (\text{OSP}^+)$$

$$\min_y S(y) \quad \text{s.t.} \quad y \in Y^+ \cap Q, \quad (\overline{\text{OSP}})$$

whose equivalence is established in (Tuan et al., 2024b, Propositions 4.3 and 4.4) when Q is a normal set. The explicit-form problem introduces the pair (x, y) :

$$\min_{(x,y)} S(\mathcal{F}(x)) \quad \text{s.t.} \quad x \in C, \quad y \in Q, \quad \mathcal{F}(x) \leq y, \quad (\text{ESP})$$

which is a pseudoconvex program when each f_i is convex (Tuan et al., 2024b, Proposition 4.5).

3.2. From ESP to Bi-Level Scalarized Split Problem

Problem (ESP) is solvable by standard gradient methods but requires the auxiliary variable y , and the coupling constraint $\mathcal{F}(x) \leq y$ can slow convergence in high dimensions. We propose a more direct formulation by eliminating y through the extended downward hull Q^+ (Definition 2.4).

Proposition 3.1. *The image-feasibility condition of (ESP)—namely, $\exists y \in Q$ with $\mathcal{F}(x) \leq y$ —is equivalent to $\mathcal{F}(x) \in Q^+$.*

PROOF. If $\mathcal{F}(x) \leq y$ with $y \in Q$, then $\mathcal{F}(x) = y - (y - \mathcal{F}(x)) \in Q - \mathbb{R}_+^m = Q^+$. Conversely, if $\mathcal{F}(x) \in Q^+$, write $\mathcal{F}(x) = y_0 - u_0$ with $y_0 \in Q, u_0 \geq 0$; then $\mathcal{F}(x) \leq y_0 \in Q$.

Replacing S by the Chebyshev scalarization (1) and using Proposition 3.1, we arrive at the *Bi-Level Scalarized Split Problem*:

$$\min_{x \in \mathbb{R}^n} s(\mathcal{F}(x), \mathbf{r}) \quad \text{subject to} \quad x \in C, \quad \mathcal{F}(x) \in Q^+. \quad (\text{BSSP})$$

Remark 3.1.1 (Relation to (Tuan et al., 2024b)). Problem (BSSP) is equivalent to (ESP) with S replaced by the Chebyshev function, but avoids the auxiliary variable y by encoding the split feasibility constraint directly through Q^+ . This simplification enables a clean three-component penalty decomposition (Section 4.1) and a transparent correspondence with the hypernetwork training loss (Section 5).

We introduce three component functions that will drive the algorithm:

$$\varphi(x) := s(\mathcal{F}(x), \mathbf{r}) = \max_{i=1, \dots, m} r_i (f_i(x) - z_i^*), \quad (5)$$

$$H(x) := \frac{1}{2} \text{dist}^2(x, C), \quad (6)$$

$$G(x) := \frac{1}{2} \text{dist}^2(\mathcal{F}(x), Q^+). \quad (7)$$

The feasible set of (BSSP) is $S := \{x \in \mathbb{R}^n : H(x) = 0, G(x) = 0\}$, the optimal value is $\varphi^* := \inf\{\varphi(x) : x \in S\}$, and the solution set is $\Omega := \{x \in S : \varphi(x) = \varphi^*\}$.

A central ingredient of the algorithm is a computable *lower bound* for φ^* . Define

$$\varphi_{\text{lb}} := \inf_{x \in C} \varphi(x). \quad (8)$$

Since $S \subset C$, every feasible point of (BSSP) belongs to C , so

$$\varphi_{\text{lb}} \leq \varphi^*. \quad (9)$$

Problem (8) is a convex program (minimization of the pointwise maximum of convex functions over a convex set) and can be solved—or approximated to arbitrary precision—by standard methods (Bertsekas, 1999; Nesterov, 2004). We write

$$\sigma := \varphi^* - \varphi_{\text{lb}} \geq 0 \quad (10)$$

for the *bound gap*. The algorithm uses only φ_{lb} (never φ^* itself).

4. Algorithm and convergence analysis

4.1. Algorithm and assumptions

At iteration k , define

$$p^k := P_{Q^+}(\mathcal{F}(x^k)), \quad \rho^k := \mathcal{F}(x^k) - p^k \geq 0, \quad (11)$$

and the direction vectors

$$z^k := x^k - P_C(x^k), \quad (12)$$

$$v^k := J_{\mathcal{F}}(x^k)^T \rho^k, \quad (13)$$

$$w^k := r_{i^*} \nabla f_{i^*}(x^k), \quad i^* \in \arg \max_i r_i (f_i(x^k) - z_i^*). \quad (14)$$

When the $\arg \max$ in (14) is not a singleton, any choice of i^* yields a valid subgradient $w^k \in \partial \varphi(x^k)$ (see Lemma 4.2 below), so the algorithm is well-defined regardless of the tie-breaking rule.

The three direction vectors have clear roles: w^k drives *optimality* (descent of the Chebyshev scalarization), z^k enforces *set feasibility* ($x \in C$), and v^k enforces *image feasibility* ($\mathcal{F}(x) \in Q^+$).

Set $\Delta_k := \varphi(x^k) - \varphi_{\text{lb}}$. The *adaptive composite direction* is

$$d^k := \alpha_k \mathbf{1}_{\{\Delta_k \geq 0\}} w^k + \beta_k z^k + \gamma_k v^k. \quad (15)$$

Since $\varphi_{\text{lb}} \leq \varphi^* \leq \varphi(x)$ for $x \in S$, the indicator equals 1 at every feasible iterate.

Algorithm 1 Adaptive balanced penalty (ABP) method

Require: $x^0 \in \mathbb{R}^n$; $r \in \mathbb{R}_{>0}^m$; $\varphi_{\text{lb}} \leq \varphi^*$; $\mu > 0$; $\{\alpha_k\}, \{\beta_k\}, \{\gamma_k\}, \{\lambda_k\}$.
 1: **for** $k = 0, 1, 2, \dots$ **do**
 2: Compute p^k, ρ^k via (11); z^k, v^k, w^k via (12)–(14);
 3: $\Delta_k \leftarrow \varphi(x^k) - \varphi_{\text{lb}}$;
 4: d^k via (15); $\eta_k \leftarrow \max(\mu, \|d^k\|)$;
 5: $x^{k+1} \leftarrow x^k - \frac{\lambda_k}{\eta_k} d^k$;
 6: **end for**

Assumption 1.

- (A1) $\mathcal{F} = (f_1, \dots, f_m) \in C^1(\mathbb{R}^n; \mathbb{R}^m)$.
- (A2) $C \subset \mathbb{R}^n$ is nonempty, closed and convex; $Q \subset \mathbb{R}^m$ is nonempty, closed and convex; $z_i^* > -\infty$ for each i .
- (A3) Each f_i is convex.
- (A4) $\Omega \neq \emptyset$, i.e., the solution set of (BSSP) is nonempty.
- (A5) $\{\lambda_k\} \subset (0, \infty)$, $\sum \lambda_k = \infty$, $\sum \lambda_k^2 < \infty$.
- (A6) $0 < \underline{\alpha} \leq \alpha_k \leq \bar{\alpha}$, $0 < \underline{\beta} \leq \beta_k \leq \bar{\beta}$, $0 < \underline{\gamma} \leq \gamma_k \leq \bar{\gamma}$ for all k .
- (A7) (Zero-gap condition). $\varphi_{\text{lb}} = \varphi^*$ (equivalently, $\sigma = 0$).

Assumptions (A1)–(A3) are standard regularity and convexity conditions. Assumption (A5) is the classical Robbins–Monro step-size condition (Robbins and Monro, 1951), satisfied by $\lambda_k = 1/(k+1)$. Assumption (A6) allows the penalty weights to be fixed constants. Assumption (A4) holds whenever C is bounded and $S \neq \emptyset$.

Weakened zero-gap condition. When the zero-gap condition (A7) cannot be verified exactly, we replace it with the following two weaker assumptions.

Assumption 2 (Bounded gap (A7')). $\sigma := \varphi^* - \varphi_{\text{lb}} \leq \varepsilon_0$ for some known constant $\varepsilon_0 \geq 0$.

Assumption 3 (Boundedness (A8)). The sequence $\{x^k\}$ generated by the ABP algorithm is bounded: $\sup_k \|x^k\| \leq B < \infty$.

Remark 4.0.1. When $\varepsilon_0 = 0$, Assumption (A7') reduces to (A7) and Assumption (A8) is a *consequence* of the quasi-Fejér property (Proposition 4.11) rather than an independent requirement. When $C \subset \mathbb{R}^n$ is compact—as is the case for CVX1 and CVX2, where C is a closed box—Assumption (A8) holds automatically for any initialization $x^0 \in C$ and need not be imposed separately. In general, (A8) can be enforced by projecting iterates onto a sufficiently large ball, or verified a posteriori for a specific instance.

Remark 4.0.2 (Assumption (A3) and non-convex problems). Convexity of each f_i is essential for Theorem 4.17: it ensures φ is convex and that the surrogate (Lemma 4.4) is a valid global minorant. The ABP algorithm is applied as an effective heuristic for non-convex objectives (e.g., the ZDT benchmarks of Section 6).

4.2. Convergence results

4.2.1. Key gradient inequalities

We collect properties of φ , H , G and construct a convex surrogate for the non-convex function G .

Lemma 4.1. *Under (A2), H is convex and C^1 with $\nabla H(x) = x - P_C(x)$. (Proof in Appendix A.1.)*

This means $z^k = \nabla H(x^k)$, so the set-feasibility step in the ABP algorithm is precisely a gradient descent step on H .

Lemma 4.2. *Under (A1) and (A3), φ is convex and $w^k \in \partial\varphi(x^k)$ for every choice of i^* in (14). (Proof in Appendix A.1.)*

This confirms that the ABP algorithm is well-defined regardless of which active index i^ is selected at each iteration.*

Since $G(x) = \frac{1}{2}\text{dist}^2(\mathcal{F}(x), \mathcal{Q}^+)$ is generally non-convex, we construct at each iteration a convex surrogate that matches G in value and gradient at x^k and minorizes G globally.

Define the *linearized half-space*

$$\mathcal{Q}_k^+ := \{y \in \mathbb{R}^m : \langle \rho^k, y - p^k \rangle \leq 0\}, \quad (16)$$

and the *convex surrogate* $\delta_k(x) := \frac{1}{2}\text{dist}^2(\mathcal{F}(x), \mathcal{Q}_k^+)$. When $\rho^k \neq 0$, the half-space projection formula (Bauschke and Combettes, 2017, Example 28.16) gives

$$\delta_k(x) = \frac{[\langle \rho^k, \mathcal{F}(x) - p^k \rangle]_+^2}{2\|\rho^k\|^2}, \quad (17)$$

when $\rho^k = 0$, $\delta_k \equiv 0$.

Lemma 4.3. *$\mathcal{Q}^+ \subseteq \mathcal{Q}_k^+$ for every k . (Proof in Appendix A.1.)*

The half-space \mathcal{Q}_k^+ contains \mathcal{Q}^+ , ensuring the surrogate δ_k globally minorizes G .

Lemma 4.4. *Under (A1) and (A3), δ_k is convex. (Proof in Appendix A.1.)*

Convexity of δ_k is the key property that makes the global subgradient inequality in Lemma 4.8 possible.

Lemma 4.5. *For every k : $\delta_k(x^k) = G(x^k)$, and $\nabla\delta_k(x^k) = v^k$ (with $v^k = 0$ when $\rho^k = 0$). (Proof in Appendix A.1.)*

The surrogate δ_k agrees with G in both value and gradient at x^k , so no approximation error is introduced at the current iterate.

The next three lemmas show that each direction vector has a useful inner-product lower bound with respect to any $x^* \in \Omega$.

Lemma 4.6. *Under (A1), (A3), (A7): $\langle w^k, x^k - x^* \rangle \geq \Delta_k$ for all k and $x^* \in \Omega$. (Proof in Appendix A.1.)*

Lemma 4.7. *Under (A2): $\langle z^k, x^k - x^* \rangle \geq H_k \geq 0$ for all k and $x^* \in \Omega$. (Proof in Appendix A.1.)*

Lemma 4.8. *Under (A1)–(A3), v^k satisfies a global subgradient inequality for G :*

$$G(y) \geq G_k + \langle v^k, y - x^k \rangle \quad \forall y \in \mathbb{R}^n, \quad k \geq 0. \quad (18)$$

In particular, $\langle v^k, x^k - x^ \rangle \geq G_k \geq 0$ for all $x^* \in \Omega$. (Proof in Appendix A.1.)*

These three inequalities are the load-bearing elements of the Lyapunov analysis: each direction vector w^k , z^k , v^k produces an inner product with $x^k - x^$ that is quantitatively lower-bounded by the corresponding sub-optimality measure Δ_k , H_k , G_k respectively.*

4.2.2. The Lyapunov function and boundedness

Throughout, $H_k := H(x^k)$, $G_k := G(x^k)$, $\Delta_k := \varphi(x^k) - \varphi_{\text{lb}}$. All estimates in this subsection hold for every $x^* \in \Omega$.

The *adaptive merit function* is

$$\Phi_k := \alpha_k \Delta_k^+ + \beta_k H_k + \gamma_k G_k, \quad \Delta_k^+ := \max(\Delta_k, 0) \geq 0. \quad (19)$$

Lemma 4.9 (Lyapunov inequality). *Under Assumption 1, for every $x^* \in \Omega$ and $k \geq 0$,*

$$\|x^{k+1} - x^*\|^2 \leq \|x^k - x^*\|^2 - \frac{2\lambda_k}{\eta_k} \Phi_k + \lambda_k^2. \quad (20)$$

(Proof in Appendix A.2.)

Lemma 4.10 (Robbins–Siegmund (Robbins and Siegmund, 1971, Lemma 1)). *If $\{a_k\}, \{b_k\} \subset [0, \infty)$ satisfy $a_{k+1} \leq a_k + b_k$ for all k and $\sum b_k < \infty$, then $\{a_k\}$ converges.*

Proposition 4.11 (Quasi-Fejér property). *Under Assumption 1, the sequence $\{\|x^k - x^*\|^2\}$ converges for every $x^* \in \Omega$; in particular, $\{x^k\}$ is bounded. (Proof in Appendix A.2.)*

Remark 4.11.1. The Lyapunov inequality (20) requires only $\eta_k \geq \|d^k\|$, which is built into the ABP algorithm. Boundedness of $\{x^k\}$ (Proposition 4.11) is therefore established prior to—and independently of—any bound on $\{d^k\}$.

Lemma 4.12. *Under Assumption 1, $\|d^k\| \leq \bar{M} < \infty$ for all k , and $\mu \leq \eta_k \leq \bar{\eta} := \max(\mu, \bar{M})$. (Proof in Appendix A.2.)*

4.2.3. Convergence theorems

The proof of global convergence proceeds in three stages. First, the Lyapunov inequality (Lemma 4.9) and the Robbins–Monro summability of $\{\lambda_k^2\}$ yield $\sum \lambda_k \Phi_k < \infty$, which forces $\liminf_{k \rightarrow \infty} \Phi_k = 0$. Second, any subsequence along which $\Phi_k \rightarrow 0$ is shown to drive all three penalty components (Δ_k^+, H_k, G_k) to zero simultaneously. Third, a convergent sub-subsequence is extracted using boundedness (Proposition 4.11), and uniqueness of the limit follows from the quasi-Fejér property.

Lemma 4.13. $\sum_{k=0}^{\infty} \lambda_k \Phi_k < \infty$. (Proof in Appendix A.3.)

Lemma 4.14. $\liminf_{k \rightarrow \infty} \Phi_k = 0$. (Proof in Appendix A.3.)

Proposition 4.15. *There exists a subsequence $\{k_j\}$ with $\Delta_{k_j}^+ \rightarrow 0$, $H_{k_j} \rightarrow 0$, $G_{k_j} \rightarrow 0$, and $\Delta_{k_j} \rightarrow 0$. (Proof in Appendix A.3.)*

Proposition 4.16. *There exist a subsequence $\{k_j\}$ and $x^\infty \in \Omega$ with $x^{k_j} \rightarrow x^\infty$. (Proof in Appendix A.3.)*

Theorem 4.17 (Global convergence). *Under Assumption 1, $\{x^k\}$ generated by the ABP algorithm (Algorithm 1) converges to some $x^\infty \in \Omega$. (Proof in Appendix A.3.)*

Remark 4.17.1. Theorem 4.17 relies on the zero-gap condition (A7). The remainder of this section extends the analysis to the case $\sigma > 0$, deriving quantitative approximate-feasibility and approximate-optimality bounds that vanish as $\varepsilon_0 \rightarrow 0$.

When only the weaker Assumption (A7') holds ($\sigma \leq \varepsilon_0$), the Lyapunov inequality acquires a drift term proportional to $\bar{\alpha}\sigma\lambda_k/\mu$, which prevents the Robbins–Siegmund argument from establishing boundedness; hence Assumption (A8) is now required. An ergodic (Cesàro) bound replaces the exact summability, yielding $\liminf_k \Phi_k \leq C_*\varepsilon_0$, and the three feasibility/optimality bounds follow by decomposing Φ_k into its nonnegative components.

When (A7) holds exactly, Theorem 4.17 guarantees full-sequence convergence to a point in Ω . The following results establish what can be concluded when only the weaker Assumption (A7') is available, replacing the Robbins–Siegmund quasi-Fejér argument with an ergodic (Cesàro) bound.

Recall the notation: $\varphi(x) = \max_i r_i(f_i(x) - z_i^*)$, $\varphi_{\text{lb}} := \inf_{x \in C} \varphi(x)$, $\sigma := \varphi^* - \varphi_{\text{lb}} \geq 0$; $H_k := \frac{1}{2} \text{dist}^2(x^k, C)$, $G_k := \frac{1}{2} \text{dist}^2(\mathcal{F}(x^k), \mathcal{Q}^+)$, $\Delta_k := \varphi(x^k) - \varphi_{\text{lb}}$; $\Phi_k := \alpha_k \Delta_k^+ + \beta_k H_k + \gamma_k G_k \geq 0$, $\Delta_k^+ := \max(\Delta_k, 0)$.

Under (A8), Lemma 4.12 (boundedness of directions) holds with $K := \bar{B}(0, B+1)$ playing the role of the compact set, giving the uniform bound $\|d^k\| \leq \bar{M} < \infty$ and hence $\mu \leq \eta_k \leq \bar{\eta} := \max(\mu, \bar{M})$ for all k .

Lemma 4.18 (Modified optimality inner product). Let $x^* \in \Omega$. Under (A1), (A3), (A7'):

$$\langle w^k, x^k - x^* \rangle \geq \Delta_k - \sigma \quad \forall k \geq 0. \quad (21)$$

(Proof in Appendix A.4.)

Lemma 4.19 (Modified Lyapunov inequality). Under (A1)–(A6), (A7'), (A8), for every $x^* \in \Omega$,

$$\|x^{k+1} - x^*\|^2 \leq \|x^k - x^*\|^2 - \frac{2\lambda_k}{\eta_k} \Phi_k + \frac{2\bar{\alpha}\sigma}{\mu} \lambda_k + \lambda_k^2 \quad \forall k \geq 0. \quad (22)$$

(Proof in Appendix A.4.)

Lemma 4.20 (Ergodic bound). Under (A1)–(A6), (A7'), (A8), define $C_* := \bar{\alpha}\bar{\eta}/\mu$ and $\Lambda_N := \sum_{k=0}^N \lambda_k$. Then

$$\limsup_{N \rightarrow \infty} \frac{1}{\Lambda_N} \sum_{k=0}^N \lambda_k \Phi_k \leq C_* \varepsilon_0, \quad (23)$$

and in particular

$$\liminf_{k \rightarrow \infty} \Phi_k \leq C_* \varepsilon_0. \quad (24)$$

(Proof in Appendix A.4.)

Proposition 4.21 (Approximate simultaneous bounds). Under (A1)–(A6), (A7'), (A8), there exist a subsequence $\{k_j\}_{j \geq 1} \subset \mathbb{N}$ and a constant $\ell_* \in [0, C_* \varepsilon_0]$ such that $\Phi_{k_j} \rightarrow \ell_*$ and, along this subsequence,

$$H_{k_j} \leq \frac{\Phi_{k_j}}{\underline{\beta}} \xrightarrow{j \rightarrow \infty} \frac{\ell_*}{\underline{\beta}} \leq \frac{C_* \varepsilon_0}{\underline{\beta}}, \quad (25)$$

$$G_{k_j} \leq \frac{\Phi_{k_j}}{\underline{\gamma}} \xrightarrow{j \rightarrow \infty} \frac{\ell_*}{\underline{\gamma}} \leq \frac{C_* \varepsilon_0}{\underline{\gamma}}, \quad (26)$$

$$\Delta_{k_j}^+ \leq \frac{\Phi_{k_j}}{\underline{\alpha}} \xrightarrow{j \rightarrow \infty} \frac{\ell_*}{\underline{\alpha}} \leq \frac{C_* \varepsilon_0}{\underline{\alpha}}. \quad (27)$$

In particular, when $\varepsilon_0 = 0$ we have $\ell_* = 0$ and $H_{k_j} \rightarrow 0$, $G_{k_j} \rightarrow 0$, $\Delta_{k_j}^+ \rightarrow 0$. (Proof in Appendix A.4.)

Theorem 4.22 (Approximate convergence). Under (A1)–(A6), (A7'), (A8), let $C_* = \bar{\alpha}\bar{\eta}/\mu$ and let $\{k_j\}$, ℓ_* be as in Proposition 4.21. Every cluster point \hat{x} of $\{x^{k_j}\}$ satisfies:

(i) (Approximate feasibility in C .)

$$H(\hat{x}) := \frac{1}{2} \text{dist}^2(\hat{x}, C) \leq \frac{\ell_*}{\underline{\beta}} \leq \frac{C_* \varepsilon_0}{\underline{\beta}}, \quad \text{i.e., } \text{dist}(\hat{x}, C) \leq \sqrt{\frac{2C_* \varepsilon_0}{\underline{\beta}}}.$$

(ii) (Approximate split feasibility.)

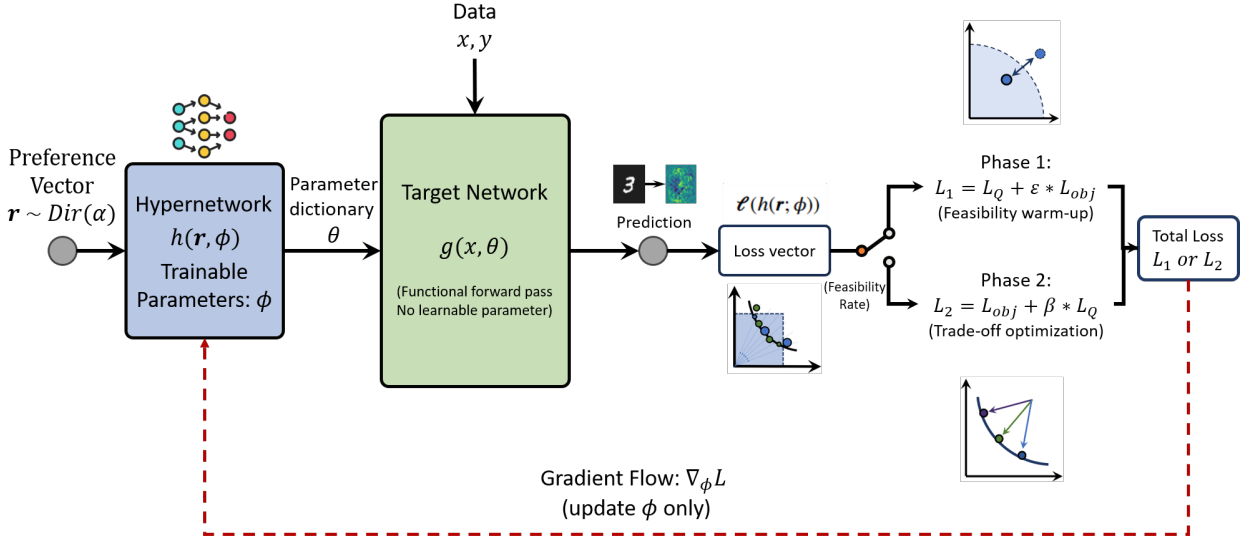
$$G(\hat{x}) := \frac{1}{2} \text{dist}^2(\mathcal{F}(\hat{x}), \mathcal{Q}^+) \leq \frac{\ell_*}{\underline{\gamma}} \leq \frac{C_* \varepsilon_0}{\underline{\gamma}}, \quad \text{i.e., } \text{dist}(\mathcal{F}(\hat{x}), \mathcal{Q}^+) \leq \sqrt{\frac{2C_* \varepsilon_0}{\underline{\gamma}}}.$$

(iii) (Approximate optimality.)

$$\varphi(\hat{x}) \leq \varphi_{\text{lb}} + \frac{\ell_*}{\underline{\alpha}} \leq \varphi^* + \frac{C_* \varepsilon_0}{\underline{\alpha}}.$$

Property	$\varepsilon_0 = 0$	$\varepsilon_0 > 0$
$\text{dist}(\hat{x}, C)$	$= 0$ (exact)	$\leq \sqrt{2C_*\varepsilon_0/\beta}$
$\text{dist}(\mathcal{F}(\hat{x}), Q^+)$	$= 0$ (exact)	$\leq \sqrt{2C_*\varepsilon_0/\gamma}$
$\varphi(\hat{x}) - \varphi^*$	$= 0$ (exact)	$\leq C_*\varepsilon_0/\alpha$
Convergence type	Full sequence (Thm. 4.17)	Subsequential
Boundedness (A8)	Consequence of analysis	Must be assumed

Table 1

 Convergence conclusions as a function of ε_0 .

Figure 2: Training pipeline for hypernetwork-based CPFL under split feasibility conditions.

When $\varepsilon_0 = 0$: $\ell_* = 0$, all three bounds vanish, and $\hat{x} \in \Omega$ (exact optimality and feasibility). (Proof in Appendix A.4.)

Remark 4.22.1 (Summary of convergence conclusions). Table 1 contrasts the conclusions for $\varepsilon_0 = 0$ and $\varepsilon_0 > 0$.

Remark 4.22.2 (Sharpness and parameter sensitivity). The constant $C_* = \bar{\alpha}\bar{\eta}/\mu$ governs the approximation quality in all three bounds. It grows with the upper bound $\bar{\alpha}$ on the optimality weight sequence and with $\bar{\eta} = \max(\mu, \bar{M})$, and decreases as the normalizer floor μ increases. Since the feasibility errors scale as $O(\sqrt{\varepsilon_0})$ and the optimality error scales as $O(\varepsilon_0)$, reducing the bound gap σ (e.g., by tightening the lower-bound computation) yields a quadratically faster improvement in feasibility quality and a linear improvement in objective quality.

Remark 4.22.3 (Recovery of exact convergence at $\varepsilon_0 = 0$). When $\varepsilon_0 = 0$ (i.e., the zero-gap condition (A7) holds), all drift contributions vanish, Assumption (A8) is superfluous, and the ergodic bound tightens to $\liminf_k \Phi_k = 0$. Theorem 4.22 then yields $\hat{x} \in \Omega$ exactly. Invoking the full-sequence convergence argument (Proposition 4.11 and Theorem 4.17) further shows that the *entire* sequence $\{x^k\}$ converges to \hat{x} .

5. Controllable Pareto front learning for multi-task learning

We now translate the ABP penalty framework into a practical training procedure for hypernetwork-based CPFL in the multi-task learning (MTL) setting. Figure 2 illustrates the overall pipeline.

Table 2

Structural correspondence between the ABP algorithm (Algorithm 1) and the hypernetwork training loss. The penalty terms and their roles map directly between the two settings; the weight schedules are discussed in Section 5.3.

ABP algorithm	Hypernetwork training	Role
$x \in \mathbb{R}^n$	$\theta = h(\mathbf{r}; \phi) \in \mathbb{R}^{n_\theta}$	Decision variable
$C \subseteq \mathbb{R}^n$	$C \subseteq \mathbb{R}^{n_\theta}$ (weight space)	Source constraint
$\mathcal{F}(x)$	$\mathcal{L}(h(\mathbf{r}; \phi))$	Objective vector
$s(\mathcal{F}(x), \mathbf{r})$	\mathcal{L}_{obj}	Chebyshev scalarization
$G(x) = \frac{1}{2} \text{dist}^2(\mathcal{F}(x), \mathcal{Q}^+)$	$\mathcal{L}_{\mathcal{Q}}$	Image-feasibility penalty
$H(x) = \frac{1}{2} \text{dist}^2(x, C)$	$\frac{1}{2} \text{dist}^2(\theta, C)$	Set-feasibility penalty

5.1. Multi-task learning as constrained multi-objective optimization

Consider m learning tasks with losses $\ell_1(\theta), \dots, \ell_m(\theta)$, where $\theta \in C$ denotes the parameters of a shared *target network* and $C \subseteq \mathbb{R}^{n_\theta}$ is the admissible parameter space. The MTL problem is naturally a multi-objective program:

$$\min_{\theta \in C} (\ell_1(\theta), \dots, \ell_m(\theta)).$$

In the CPFL paradigm, a *hypernetwork* $h(\mathbf{r}; \phi): \mathbb{R}^m \rightarrow \mathbb{R}^{n_\theta}$ takes a preference vector $\mathbf{r} \in \Delta^{m-1}$ (the probability simplex) as input and produces the target network parameters $\theta_{\mathbf{r}} = h(\mathbf{r}; \phi)$. A single set of hypernetwork parameters ϕ thus parametrizes the entire Pareto front.

Combining CPFL with the split feasibility framework of (Tuan et al., 2024b), the training problem is:

$$\phi^* = \arg \min_{\phi} \mathbb{E}_{\mathbf{r} \sim \text{Dir}(\alpha)} \left[\max_{i=1, \dots, m} \{r_i (\ell_i(h(\mathbf{r}; \phi)) - a_i)\} \right] \quad \text{s.t.} \quad h(\mathbf{r}; \phi) \in C, \quad \mathcal{L}(h(\mathbf{r}; \phi)) \in \mathcal{Q}, \quad (28)$$

where $\mathcal{L} = (\ell_1, \dots, \ell_m)$, a_i is the ideal loss for task i , and \mathcal{Q} is the decision-maker's preferred region in the loss space. In the notation of (BSSP), the variable is $x := h(\mathbf{r}; \phi) \in \mathbb{R}^{n_\theta}$, the objective mapping is $\mathcal{F} := \mathcal{L}$, the source constraint is $C \subseteq \mathbb{R}^{n_\theta}$, and the target constraint is $\mathcal{Q} \subset \mathbb{R}^m$. In practice, $C = \mathbb{R}^{n_\theta}$ (unconstrained weight space), so the set-feasibility penalty $H(\theta) = \frac{1}{2} \text{dist}^2(\theta, C)$ vanishes identically; we retain C in the formulation to preserve the structural correspondence with the ABP algorithm.

Different MTL problems use different target network architectures (see Section 7); the hypernetwork architectures described below are agnostic to the choice of target network.

5.2. Hypernetwork architectures

Both hypernetwork architectures generate the full parameter dictionary $\theta = \{\theta_j\}$ of a purely functional *target network* $g(\cdot; \theta)$ that holds no learnable parameters of its own; all weights are injected at run-time so that gradients flow from the task losses back to the hypernetwork parameters ϕ . For the MTL experiments, the target network is a Multi-LeNet CNN (Sener and Koltun, 2018; Navon et al., 2021) (Fig. 3), comprising $|\theta| = 31,910$ parameters (two conv-pool blocks, one hidden layer, two task-specific heads). The hypernetwork size is $|\phi| \approx 8.66$ M for both architectures, following (Tuan et al., 2024b).

5.2.1. Hyper-MLP

The MLP-based hypernetwork (Navon et al., 2021) processes the preference vector as a single input and maps it through a shared trunk to per-parameter linear heads. Given $\mathbf{r} \in \mathbb{R}^m$, the shared representation is:

$$\mathbf{h}_{\text{MLP}}(\mathbf{r}) = \text{ReLU}(\mathbf{W}_3 \text{ReLU}(\mathbf{W}_2 \text{ReLU}(\mathbf{W}_1 \mathbf{r} + \mathbf{b}_1) + \mathbf{b}_2) + \mathbf{b}_3) \in \mathbb{R}^d, \quad (29)$$

where $d = 256$ is the hidden dimension and $\mathbf{W}_1 \in \mathbb{R}^{d \times m}$, $\mathbf{W}_2, \mathbf{W}_3 \in \mathbb{R}^{d \times d}$ are learnable weight matrices with corresponding biases. Each target parameter θ_j is produced by a dedicated linear head:

$$\theta_j = \mathbf{A}_j \mathbf{h}_{\text{MLP}}(\mathbf{r}) + \mathbf{c}_j, \quad \mathbf{A}_j \in \mathbb{R}^{n_j \times d}, \quad \mathbf{c}_j \in \mathbb{R}^{n_j}. \quad (30)$$

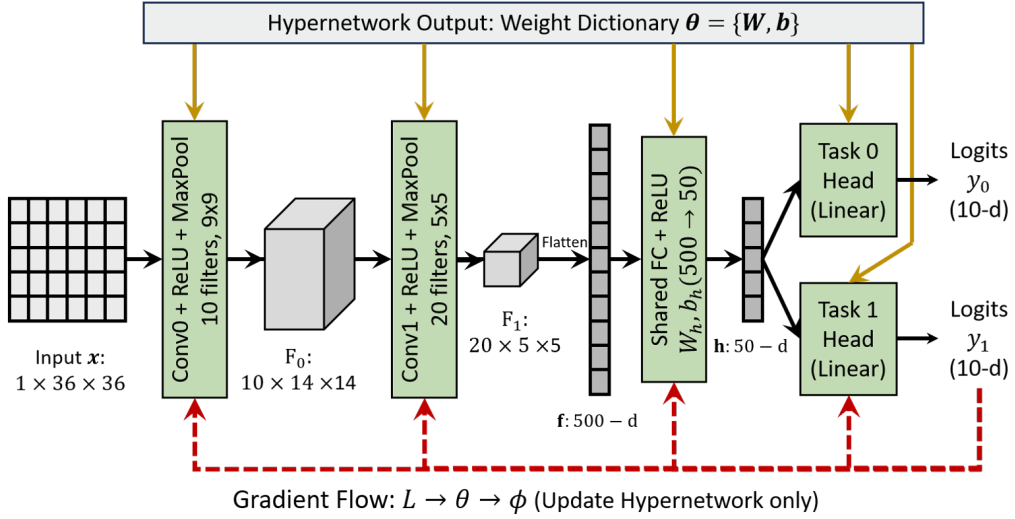


Figure 3: Multi-LeNet target network for Multi-MNIST, Multi-Fashion, and Fashion+MNIST. All weights θ are generated by the hypernetwork; no learnable parameters reside in the target network itself. The two task heads produce logits for the left-image task (Task 0) and right-image task (Task 1), respectively.

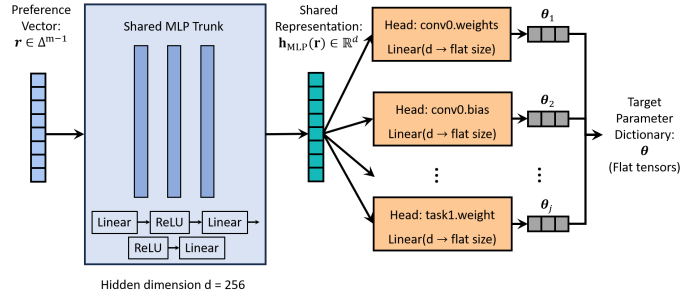


Figure 4: Hyper-MLP architecture. A three-layer shared MLP trunk maps \mathbf{r} to $\mathbf{h}_{\text{MLP}}(\mathbf{r}) \in \mathbb{R}^d$; separate linear heads project this representation onto each target parameter tensor θ_j .

5.2.2. HyperTrans

The key limitation of Hyper-MLP is that \mathbf{r} is processed as a monolithic input, obscuring per-objective contributions. This matters for the BSSP penalty structure because the image feasibility residual ρ^k has a per-objective decomposition. The Transformer-based hypernetwork (Tuan et al., 2024b) addresses this by treating each component r_i as a separate *token*, enabling explicit pairwise interaction through self-attention—a design motivated by the universal approximation properties of Transformers (Yun et al., 2020).

Per-component embedding. Each $r_i \in \mathbb{R}$ is mapped to a d -dimensional embedding:

$$\mathbf{e}_i = \text{act}(\mathbf{U}_i r_i + \mathbf{d}_i) \in \mathbb{R}^d, \quad i = 1, \dots, m, \quad (31)$$

where $\mathbf{U}_i \in \mathbb{R}^{d \times 1}$, $\mathbf{d}_i \in \mathbb{R}^d$. The embeddings are stacked into $\mathbf{E} = [\mathbf{e}_1, \dots, \mathbf{e}_m]^T \in \mathbb{R}^{m \times d}$.

Transformer block. A single Transformer block with multi-head self-attention (MHSA) and a feed-forward network (FFN), each with residual connections, processes the sequence:

$$\mathbf{E}' = \mathbf{E} + \text{MHSA}(\mathbf{E}, \mathbf{E}, \mathbf{E}), \quad (32)$$

$$\mathbf{E}'' = \mathbf{E}' + \text{FFN}(\mathbf{E}'). \quad (33)$$

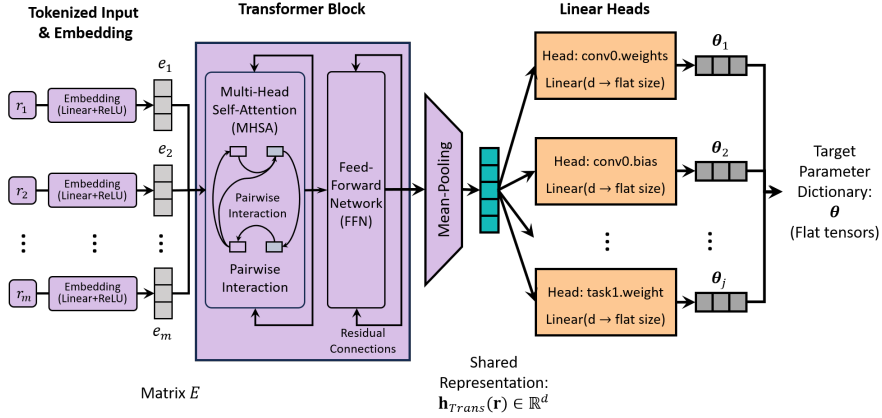


Figure 5: HyperTrans architecture: each r_i is embedded into a d -dimensional token; a single Transformer block captures pairwise interactions; mean-pooling aggregates the tokens into a shared state projected via linear heads to produce θ .

The attention scores capture the pairwise trade-off structure, providing HyperTrans with an inductive bias for modelling the coupling between objectives—precisely what the image-feasibility direction $v^k = J_{\mathcal{F}}(x^k)^T \rho^k$ aggregates in the ABP algorithm.

Aggregation. The processed tokens are aggregated by mean-pooling:

$$\mathbf{h}_{\text{Trans}}(\mathbf{r}) = \frac{1}{m} \sum_{i=1}^m \mathbf{E}_i'' \in \mathbb{R}^d, \quad (34)$$

followed by the same per-parameter linear heads as in (30).

Table 2 makes the structural correspondence between the ABP algorithm and the hypernetwork training loss explicit.

5.3. Two-phase feasibility-first training

Scope of the training strategy. Theorem 4.17 guarantees full-sequence convergence of the ABP algorithm to an optimal BSSP solution under Assumption 1, which includes convexity of each f_i , Robbins–Monro step-sizes, and bounded penalty weights. The hypernetwork training described below operates outside this regime: objectives are non-convex, gradients are stochastic mini-batches, and the phase transition introduces changes in the penalty weights not covered by the assumptions of Theorem 4.17. Accordingly, the two-phase strategy should be understood as a *convergence-theory-inspired heuristic*: it embodies the feasibility-first principle derived from the ABP algorithm, but its convergence properties in the neural network setting remain an open question (see Section 8).

The penalty structure of the ABP algorithm—where the feasibility weights β_k, γ_k are non-decreasing while the optimality weight α_k is non-increasing—suggests a natural analogue for hypernetwork training: first drive the generated solutions into the feasible region Q (Phase 1), then optimize the Chebyshev trade-off within Q (Phase 2).

Phase 1 (feasibility warm-up). The training loss emphasizes the constraint penalty:

$$\mathcal{L}^{(1)} = \mathcal{L}_Q + \varepsilon \mathcal{L}_{\text{obj}}, \quad (35)$$

where $\mathcal{L}_{\text{obj}} = \max_i \{r_i (\ell_i(h(\mathbf{r}; \phi)) - a_i)\}$ is the Chebyshev scalarization loss and \mathcal{L}_Q penalizes the squared violation of the constraint region Q . The dominant \mathcal{L}_Q term drives the hypernetwork outputs into the feasible region, while the small coefficient ε maintains diversity across preference vectors, preventing collapse to a single feasible point. This phase corresponds to the early iterations of the ABP algorithm, where the large γ_k on the image-feasibility direction v^k pulls the iterates towards Q^+ .

Phase 2 (trade-off optimization). Once feasibility is sufficiently established, the loss reverses the emphasis:

$$\mathcal{L}^{(2)} = \mathcal{L}_{\text{obj}} + \beta \mathcal{L}_Q, \quad (36)$$

where $\beta > 0$ is an adaptive penalty coefficient. This creates a dynamic equilibrium: when solutions drift outside Q , β is increased to restore feasibility; when feasibility is comfortable, β is relaxed to give the Chebyshev objective more

freedom. This mirrors the late iterations of the ABP algorithm, where the optimality direction w^k (weighted by α_k) becomes the primary driver while the penalty terms prevent excessive constraint violation.

Gradient flow. For each sampled preference r , the gradient path is: $r \xrightarrow{h(\cdot; \phi)} \theta_r \xrightarrow{\text{target net}} \hat{y} \xrightarrow{\text{losses}} \ell \xrightarrow{\text{scalarization}} \mathcal{L} \xrightarrow{\nabla_\phi} \phi$. Only the hypernetwork parameters ϕ are updated; the target network has no learnable parameters of its own. In both phases, the set-feasibility penalty $H \equiv 0$ is absent from the training loss, as noted in Section 5.1.

5.4. Evaluation metrics

We employ three complementary metrics; the first two are standard, while the third is introduced in this work.

Mean Euclidean Distance (MED) (Tuan et al., 2024b). When ground-truth constrained Pareto solutions are available, the MED measures approximation accuracy:

$$\text{MED}(\mathcal{F}^*, \hat{\mathcal{F}}) = \frac{1}{|\mathcal{F}^*|} \sum_{i=1}^{|\mathcal{F}^*|} \|f_i^* - \hat{f}_i\|_2. \quad (37)$$

A lower MED indicates that predicted solutions lie closer to the true constrained Pareto front.

Hypervolume (HV) (Zitzler and Thiele, 1999). Given a finite set $\mathcal{P} = \{p_j \in \mathbb{R}^m\}$ of non-dominated points and a reference point $\bar{y} \in \mathbb{R}_+^m$, the hypervolume is

$$\text{HV}(\mathcal{P}) = \text{VOL} \left(\bigcup_{p \in \mathcal{P}, p < \bar{y}} \prod_{i=1}^m [p_i, \bar{y}_i] \right). \quad (38)$$

A higher HV indicates a better-spread and better-converged Pareto front approximation.

Expected Feasible Hypervolume (EFHV). In constrained multi-objective settings, reporting HV and feasibility rate separately makes it difficult to rank methods that trade off one for the other. Feasibility-weighted hypervolume concepts have appeared in constrained Bayesian optimization, where the Constrained Expected Hypervolume Improvement (CEHVI) multiplies the Expected Hypervolume Improvement by the probability of feasibility (Emmerich et al., 2006; Gelbart et al., 2014). However, CEHVI is a *point-wise acquisition function* designed to guide sequential search, not a set-level evaluation metric. In evolutionary constrained multi-objective optimization, the standard practice is to compute HV on the feasible subset alone (Zitzler and Thiele, 1999), which ignores the feasibility rate entirely. Existing CPFL methods (Navon et al., 2021; Tuan et al., 2024b; Lin et al., 2022) report only unconstrained HV or MED and do not provide a combined quality–feasibility metric.

To address this gap, we define the *Expected Feasible Hypervolume* as a set-level evaluation metric that multiplicatively combines both dimensions. Let $\mathcal{P} = \{p_j\}_{j=1}^K$ be the solutions produced for K preference rays, and let $\pi = |\{j : p_j \in \mathcal{Q}\}|/K$ denote the ray-level feasibility rate. The EFHV is defined as

$$\text{EFHV}(\mathcal{P}) = \pi \cdot \text{HV}(\mathcal{P}_{\text{feas}}), \quad (39)$$

where $\mathcal{P}_{\text{feas}} = \{p_j \in \mathcal{Q}\}$ is the feasible subset. The multiplicative form ensures that a method must excel on *both* dimensions to achieve a high score: even if the feasible subset has high HV, a low feasibility rate π suppresses the overall EFHV proportionally.

6. Internal validation: multi-objective optimization benchmarks

6.1. Benchmark problems

We validate the ABP algorithm (Algorithm 1) and its hypernetwork-based adaptation (ABP-HyperTrans) on five benchmark problems from the literature, summarized in Table 3. The Pareto fronts are normalized to $[0, 1]^m$ following the convention of (Tuan et al., 2024b). The constraint set \mathcal{Q} is chosen as a sphere $\bar{B}(c, R) := \{y \in \mathbb{R}^m : \|y - c\| \leq R\}$ in all cases. Problem names (CVX1–CVX3, ZDT1–ZDT2) and their decision sets \mathcal{C} follow the cited sources (Tuan et al., 2024b; Binh and Korn, 1997; Thang et al., 2020; Zitzler et al., 2000); the prefix “CVX” designates problems whose *objective functions* are convex and does not imply convexity of the decision set \mathcal{C} . The target regions \mathcal{Q} listed in Table 3 are introduced in this paper.

Table 3

MOP benchmark specifications. n : number of decision variables; m : number of objectives; C : decision space; Q : target region in objective space; $\overline{B}(c, R)$ denotes the closed ball of radius R centered at c .

Problem	Source	n	m	Q	Type
CVX1	(Tuan et al., 2024b)	1	2	$\overline{B}((0.4, 0.4), 0.2)$	Convex
CVX2	(Binh and Korn, 1997)	2	2	$\overline{B}((0.4, 0.4), 0.2)$	Convex
CVX3	(Thang et al., 2020)	3	3	$\overline{B}((0.5, 0.5, 0.5), 0.2)$	Convex
ZDT1	(Zitzler et al., 2000)	30	2	$\overline{B}((0.4, 0.4), 0.2)$	Non-convex
ZDT2	(Zitzler et al., 2000)	30	2	$\overline{B}((0.4, 0.5), 0.4)$	Non-convex

6.1.1. Convex benchmarks

CVX1 (Tuan et al., 2024b). A two-objective problem in one variable:

$$\min_x \{x, (x-1)^2\} \quad \text{s.t.} \quad 0 \leq x \leq 1. \quad (\text{CVX1})$$

CVX2 (Binh and Korn, 1997). A two-objective problem in two variables (Binh–Korn problem):

$$\min_{x_1, x_2} \{f_1, f_2\} \quad \text{s.t.} \quad x_i \in [0, 5], \quad i = 1, 2, \quad (\text{CVX2})$$

where

$$f_1 = \frac{x_1^2 + x_2^2}{50}, \quad f_2 = \frac{(x_1 - 5)^2 + (x_2 - 5)^2}{50}.$$

CVX3 (Thang et al., 2020). A three-objective problem on the unit sphere in \mathbb{R}^3 . While the objective functions are convex (as indicated by the prefix), the spherical decision set C is non-convex; consequently, the convergence guarantees of Theorems 4.17 and 4.22 do not apply, and the ABP algorithm is applied to this benchmark as an effective heuristic.

$$\min_{x_1, x_2, x_3} \{f_1, f_2, f_3\} \quad \text{s.t.} \quad x_1^2 + x_2^2 + x_3^2 = 1, \quad x_i \in [0, 1], \quad i = 1, 2, 3, \quad (\text{CVX3})$$

where

$$f_1 = \frac{x_1^2 + x_2^2 + x_3^2 + x_2 - 12x_3 + 12}{14},$$

$$f_2 = \frac{x_1^2 + x_2^2 + x_3^2 + 8x_1 - 44.8x_2 + 8x_3 + 44}{57},$$

$$f_3 = \frac{x_1^2 + x_2^2 + x_3^2 - 44.8x_1 + 8x_2 + 8x_3 + 43.7}{56}.$$

6.1.2. Non-convex benchmarks

ZDT1 (Zitzler et al., 2000). A classical bi-objective benchmark with a convex Pareto front:

$$f_1(\mathbf{x}) = x_1, \quad f_2(\mathbf{x}) = g(\mathbf{x}) \left[1 - \sqrt{f_1(\mathbf{x})/g(\mathbf{x})} \right], \quad (\text{ZDT1})$$

where $g(\mathbf{x}) = 1 + \frac{9}{n-1} \sum_{i=2}^n x_i$ and $0 \leq x_i \leq 1$ for $i = 1, \dots, n$ (with $n = 30$). The analytical Pareto front satisfies $f_2 = 1 - \sqrt{f_1}$ for $f_1 \in [0, 1]$.

ZDT2 (Zitzler et al., 2000). A classical bi-objective benchmark with a non-convex Pareto front:

$$f_1(\mathbf{x}) = x_1, \quad f_2(\mathbf{x}) = g(\mathbf{x}) \left[1 - (f_1(\mathbf{x})/g(\mathbf{x}))^2 \right], \quad (\text{ZDT2})$$

where $g(\mathbf{x})$ is as in (ZDT1) and $n = 30$. The analytical Pareto front satisfies $f_2 = 1 - f_1^2$ for $f_1 \in [0, 1]$.

Since all five MOP benchmarks admit known ground-truth constrained Pareto solutions, the primary validation metric is the MED (Section 5.4); HV and EFHV are also reported.

Table 4

Internal validation on MOP benchmarks (50 preference rays). MED (\downarrow) measures distance to the ground-truth constrained Pareto front. ABP Solver reports a single deterministic run; ABP-HyperTrans reports mean \pm std over 10 seeds. **Bold**: best MED per problem.

Problem	ABP Solver		ABP-HyperTrans		Theory
	MED	Time (ms)	MED (mean \pm std)	Time (ms)	
CVX1	0.005126	1451	0.004742 \pm 0.001884	16.4	✓
CVX2	0.002773	228	0.001895 \pm 0.000246	16.6	✓
CVX3	0.007237	616	0.007156 \pm 0.000614	28.0	heuristic
ZDT1	0.009889	1802	0.006334 \pm 0.001973	17.0	heuristic
ZDT2	0.010078	12835	0.008518 \pm 0.001063	16.7	heuristic

6.2. Experimental setup

Two-phase execution. For each benchmark, the algorithm proceeds in two phases: Phase 1 uses the CQ method (4) to find an initial feasible point $x_{\text{feas}} \in S$; Phase 2 runs the ABP algorithm from x_{feas} for K uniformly spaced preference vectors on the simplex.

Ground truth. For CVX1–2, the Chebyshev-optimal points under the constraint $\mathcal{F}(x) \in Q^+$ are computed by an exact solver (SLSQP with analytical Jacobian). For CVX3, grid search on the unit sphere combined with Q^+ filtering and Chebyshev optimization is used. For ZDT1 and ZDT2, the analytical Pareto front is sampled at 5000 uniformly spaced points and filtered by Q^+ ; the resulting constrained front serves as the reference for MED computation.

Step-size schedule. All runs of the ABP algorithm use the step-size schedule $\lambda_k = 1/(k+1)^\nu$ for a problem-dependent exponent $\nu \in (1/2, 1]$, which satisfies the Robbins–Monro condition (A5) for any such choice of ν .

Verification of Assumptions (A7)–(A8). For CVX1 and CVX2 the decision set C is a compact box, so Assumption (A8) holds automatically. The zero-gap condition (A7) is verified numerically for all 50 preference rays via SLSQP; the gap σ equals zero on 39/50 rays (CVX1) and 44/50 rays (CVX2), with $\sigma_{\text{max}} \leq 0.081$. Full details are given in Appendix C.1.

6.3. Results

The purpose of this section is *internal validation*: we verify that (1) the ABP algorithm (Algorithm 1) faithfully approximates the known ground-truth constrained Pareto solutions, and (2) the hypernetwork-based adaptation (ABP-HyperTrans) matches or improves upon the numerical solver while offering orders-of-magnitude faster inference. Table 4 reports MED (\downarrow) and inference time for all five benchmarks at 50 preference rays.

Correctness of the ABP algorithm. The ABP Solver achieves low MED on all five benchmarks, confirming that the proposed penalty structure successfully balances optimality and feasibility. On CVX1 and CVX2, convergence is guaranteed by Theorem 4.17 on the majority of preference rays (Appendix C.1); on the remaining rays, Theorem 4.22 provides approximate convergence bounds. On CVX3 and the non-convex ZDT problems, the algorithm operates as an effective heuristic (Remark 4.0.2).

ABP-HyperTrans matches or improves the solver. ABP-HyperTrans achieves lower mean MED than the ABP Solver on all five benchmarks, demonstrating that the hypernetwork-based adaptation faithfully—and in some cases more accurately—approximates the ground-truth constrained Pareto front. The improvement is most pronounced on ZDT1 and ZDT2, where the self-attention mechanism captures the higher-dimensional preference-to-solution mapping more effectively.

Computational efficiency. The inference time of ABP-HyperTrans (16–28 ms) is two to three orders of magnitude faster than the ABP Solver (228–12,835 ms), confirming the practical advantage of the learned model for real-time preference control.

Figures 6 and 7 display the approximated constrained Pareto fronts produced by ABP-HyperTrans on four benchmarks with 50 preference rays. In each panel, the shaded region represents the extended downward hull Q^+ , gold dots mark the ground-truth constrained solutions, and green markers show the solutions returned by ABP-HyperTrans. The MED and HV values annotated in each panel correspond to a single representative seed; quantitative comparisons across all seeds should be drawn from Table 4.

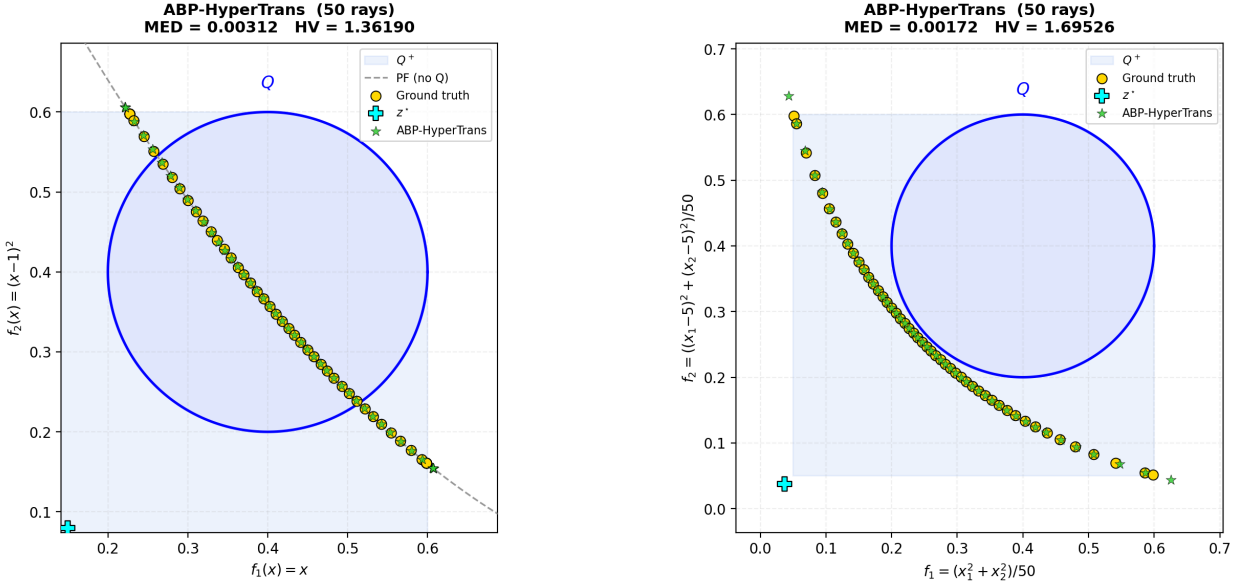


Figure 6: Constrained Pareto front approximation on two convex benchmarks with 50 rays. Left: CVX1 (dim $x = 1$). Right: CVX2 (dim $x = 2$, Binh & Korn). ABP-HyperTrans places its output points tightly along the ground-truth constrained front inside Q^+ .

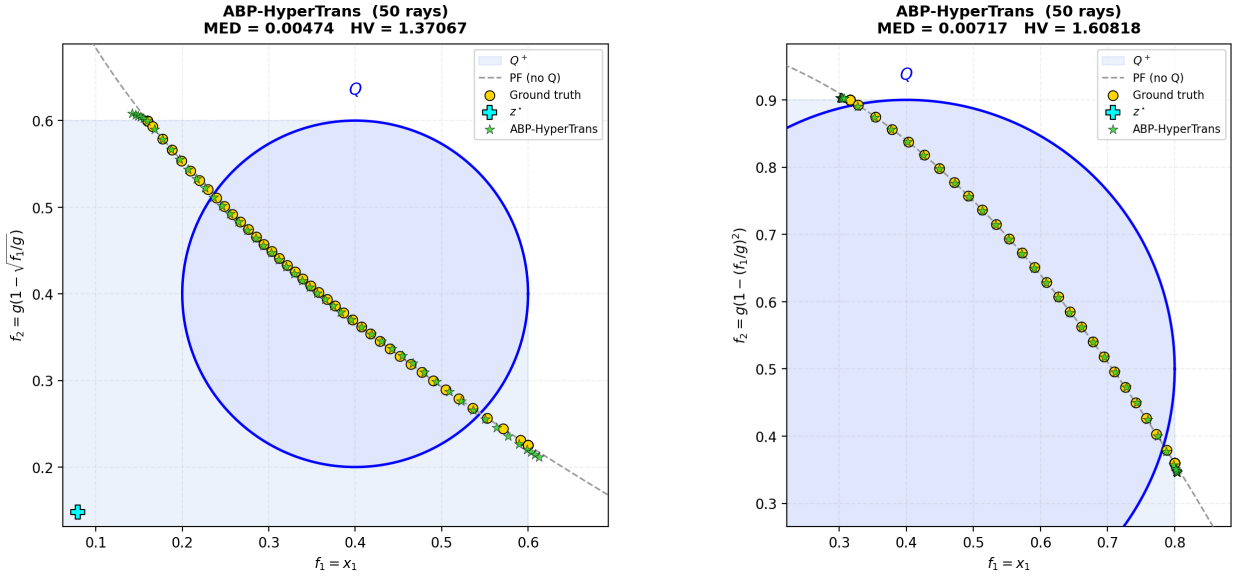


Figure 7: Constrained Pareto front approximation on two non-convex ZDT benchmarks with 50 rays. Left: ZDT1 (dim $x = 30$, convex front $f_2 = 1 - \sqrt{f_1}$). Right: ZDT2 (dim $x = 30$, concave front $f_2 = 1 - f_1^2$). Layout as in Fig. 6.

In Fig. 6, ABP-HyperTrans achieves high-fidelity approximation on both convex benchmarks. On CVX1 (left), the one-dimensional decision variable yields a clean mapping from preference rays to the constrained front, and virtually all solutions lie inside Q^+ . On CVX2 (right), the two-variable objective map produces a well-structured arc and ABP-HyperTrans tracks the ground-truth with low MED, confirming reliable satisfaction of the spherical constraint.

In Fig. 7, the 30-dimensional ZDT benchmarks present a substantially harder learning task. On ZDT1 (left), the convex unconstrained front ($f_2 = 1 - \sqrt{f_1}$) is clipped by Q , and ABP-HyperTrans successfully concentrates its solutions along the feasible arc. On ZDT2 (right), the concave shape of the unconstrained front ($f_2 = 1 - f_1^2$) interacts

Table 5

Constraint regions Q for the MTL experiments. Box: $Q = \{\ell : \ell \leq \mathbf{b}\}$; Sphere: $Q = \overline{B}(\mathbf{c}, R)$.

Dataset	Box \mathbf{b}	Sphere (\mathbf{c}, R)
Multi-MNIST	(0.30, 0.40)	$\mathbf{c} = (0.25, 0.35)$, $R = 0.05$
Multi-Fashion	(0.75, 0.75)	$\mathbf{c} = (0.65, 0.65)$, $R = 0.10$
Fashion+MNIST	(0.60, 0.60)	$\mathbf{c} = (0.50, 0.50)$, $R = 0.10$

with the spherical constraint in a non-trivial way; ABP-HyperTrans nonetheless tracks the ground-truth constrained front with only minor deviations near the boundary of Q .

We use $K = 50$ preference rays for all MOP experiments, following the convention of (Tuan et al., 2024b). Appendix C.2 reports an ablation confirming that approximation quality improves monotonically with ray count.

7. Experiments: multi-task learning

7.1. Experimental setup

We evaluate the two-phase training strategy (Section 5.3) on three image classification benchmarks from multi-task learning.

Datasets. These three benchmark datasets (Sabour et al., 2017; Xiao et al., 2017; Lin et al., 2019) are commonly used in multi-task learning. Each image is $1 \times 36 \times 36$ (single-channel) and contains two overlapping items (digits or fashion articles); the two tasks are to classify the top-left item (Task L) and the bottom-right item (Task R), each into 10 classes. Each dataset has 120 000 training and 20 000 test examples; 10% of the training set is held out for validation.

Target network and hypernetwork. The target network is the Multi-LeNet CNN described in Section 5.2 (Fig. 3), with $|\theta| = 31,910$ parameters per preference vector and hypernetwork size $|\phi| \approx 8.66 \text{ M}$ ($d = 256$), following (Tuan et al., 2024b).

Training details. We follow the ten-fold cross-validation protocol and general training configurations of (Tuan et al., 2024b) for a fair comparison. All experiments use the Adam optimizer with a learning rate of 5×10^{-4} and batch size 256. For evaluation, we employ 25 evenly spaced preference vectors on the simplex with a hypervolume reference point of (2, 2). Our proposed two-phase strategy transitions from Phase 1 to Phase 2 when the validation feasibility rate exceeds 95% (or after a maximum of 80 epochs), at which point the adaptive penalty coefficient β is introduced.

Constraint regions. Table 5 specifies the constraint regions Q used for each dataset. The Box constraint enforces per-task loss upper bounds $Q = \{\ell \in \mathbb{R}^2 : \ell \leq \mathbf{b}\}$; the Sphere constraint enforces $Q = \overline{B}(\mathbf{c}, R) = \{\ell : \|\ell - \mathbf{c}\| \leq R\}$. These regions were selected so that the constraint boundary intersects the unconstrained Pareto front near the centre of the achievable loss range on each dataset.

7.2. Results

Tables 6–8 report HV (computed on the feasible subset $\mathcal{P}_{\text{feas}}$ only), π (feasibility rate, as defined in Section 5.4), and EFHV under Box ($Q = [\mathbf{a}, \mathbf{b}]$) and Sphere ($Q = \overline{B}(\mathbf{c}, R)$) constraints, averaged over 10 folds. Since the baselines of Tuan et al. (2024a,b) do not enforce constraints during training, we evaluate their test solutions post hoc against each constraint region Q to compute π and EFHV under equal conditions.

Several consistent patterns emerge across all three datasets.

Constrained vs. unconstrained. The EFHV metric reveals the decisive advantage of constrained training. Although the unconstrained baselines achieve comparable or slightly higher HV on their feasible subsets, their π is consistently low (36–49%), resulting in EFHV values roughly 50–60% below ours. For instance, on Multi-MNIST (Box), the baseline Hyper-MLP achieves $\text{HV} = 2.974$ but only $\pi = 43.0\%$ ($\text{EFHV} = 1.282$), whereas ABP-HyperMLP reaches $\pi = 100.0\%$ with $\text{HV} = 2.958$ ($\text{EFHV} = 2.958$, a $2.3\times$ improvement). This pattern is consistent across all 12 configurations (2 architectures \times 2 constraints \times 3 datasets).

Architecture and constraint geometry. ABP-HyperMLP consistently outperforms ABP-HyperTrans in HV, suggesting that the lighter MLP hypernetwork is better suited to the two-task MTL setting. The Sphere constraint generally yields higher π than Box, likely due to its smoother projection geometry.

Qualitative visualization. Figures 8–10 compare the loss-space Pareto fronts of all four methods for a representative fold under Box (left) and Sphere (right) constraints. In each panel, the shaded region indicates the feasible

Table 6

Multi-MNIST results (mean \pm std, 10-fold CV, HV ref. point (2,2)). HV is computed on the feasible subset $\mathcal{P}_{\text{feas}}$ only. **Bold**: best π and EFHV per constraint.

Method	Constr.	HV (\uparrow)	π (%) (\uparrow)	EFHV (\uparrow)
Hyper-MLP (Tuan et al., 2024a)	Box	2.974 \pm 0.014	43.0 \pm 10.3	1.282 \pm 0.312
HyperTrans (Tuan et al., 2024b)	Box	2.955 \pm 0.015	36.5 \pm 3.7	1.078 \pm 0.108
ABP-HyperMLP (ours)	Box	2.958 \pm 0.013	100.0 \pm 0.0	2.958 \pm 0.013
ABP-HyperTrans (ours)	Box	2.959 \pm 0.007	92.5 \pm 11.0	2.737 \pm 0.327
Hyper-MLP (Tuan et al., 2024a)	Sphere	2.974 \pm 0.014	43.0 \pm 10.3	1.282 \pm 0.312
HyperTrans (Tuan et al., 2024b)	Sphere	2.955 \pm 0.015	35.5 \pm 2.4	1.049 \pm 0.070
ABP-HyperMLP (ours)	Sphere	2.968 \pm 0.010	100.0 \pm 0.0	2.968 \pm 0.010
ABP-HyperTrans (ours)	Sphere	2.955 \pm 0.008	99.5 \pm 1.3	2.940 \pm 0.036

Table 7

Multi-Fashion results (same protocol as Table 6).

Method	Constr.	HV (\uparrow)	π (%) (\uparrow)	EFHV (\uparrow)
Hyper-MLP (Tuan et al., 2024a)	Box	2.337 \pm 0.016	42.9 \pm 2.8	1.002 \pm 0.069
HyperTrans (Tuan et al., 2024b)	Box	2.201 \pm 0.028	36.6 \pm 4.5	0.805 \pm 0.110
ABP-HyperMLP (ours)	Box	2.316 \pm 0.015	94.9 \pm 8.2	2.191 \pm 0.203
ABP-HyperTrans (ours)	Box	2.196 \pm 0.016	90.3 \pm 12.3	1.984 \pm 0.280
Hyper-MLP (Tuan et al., 2024a)	Sphere	2.337 \pm 0.016	42.9 \pm 2.8	1.002 \pm 0.069
HyperTrans (Tuan et al., 2024b)	Sphere	2.201 \pm 0.028	36.6 \pm 4.5	0.805 \pm 0.110
ABP-HyperMLP (ours)	Sphere	2.322 \pm 0.012	100.0 \pm 0.0	2.322 \pm 0.012
ABP-HyperTrans (ours)	Sphere	2.195 \pm 0.020	89.1 \pm 10.4	1.957 \pm 0.230

Table 8

Fashion+MNIST results (same protocol as Table 6).

Method	Constr.	HV (\uparrow)	π (%) (\uparrow)	EFHV (\uparrow)
Hyper-MLP (Tuan et al., 2024a)	Box	2.928 \pm 0.012	49.1 \pm 1.8	1.439 \pm 0.056
HyperTrans (Tuan et al., 2024b)	Box	2.847 \pm 0.021	41.7 \pm 2.0	1.188 \pm 0.062
ABP-HyperMLP (ours)	Box	2.928 \pm 0.020	87.4 \pm 4.0	2.561 \pm 0.132
ABP-HyperTrans (ours)	Box	2.844 \pm 0.033	90.9 \pm 5.5	2.584 \pm 0.161
Hyper-MLP (Tuan et al., 2024a)	Sphere	2.928 \pm 0.012	49.1 \pm 1.8	1.439 \pm 0.056
HyperTrans (Tuan et al., 2024b)	Sphere	2.847 \pm 0.021	41.7 \pm 2.0	1.188 \pm 0.062
ABP-HyperMLP (ours)	Sphere	2.935 \pm 0.021	88.6 \pm 3.3	2.606 \pm 0.111
ABP-HyperTrans (ours)	Sphere	2.867 \pm 0.030	91.4 \pm 4.0	2.550 \pm 0.130

set Q (or Q^+ for the Sphere case), and the legend reports the ray-level feasibility rate for that fold. The unconstrained baselines (grey circles, yellow diamonds) spread well beyond Q , achieving only 36–64% feasibility. In contrast, ABP-trained solutions (red squares, green triangles) concentrate inside Q , reaching 76–100% feasibility while maintaining comparable spread along the Pareto front. Quantitative comparison across all folds should rely on the 10-fold averages in Tables 6–8; additional per-architecture visualizations under individual constraint types are provided in Appendix B.

7.3. Ablation study: training strategy

To validate the necessity of each component in the two-phase training strategy, we conduct an ablation study (ABP-HyperMLP, Box constraint, 10-fold CV) on all three datasets and report the mean across datasets in Table 9. We compare the Full strategy against four degraded variants. **No-Phase1** skips the Phase 1 feasibility warm-up and begins directly with $\mathcal{L}_{\text{obj}} + \beta \mathcal{L}_Q$ from epoch 1. **No-Adaptive- β** retains both phases but fixes the penalty coefficient ($\rho = 1.0$, so β never grows). **Single-Phase** uses a fixed $\mathcal{L}_{\text{obj}} + \beta_0 \mathcal{L}_Q$ throughout training with no phase transition and

Multi-MNIST

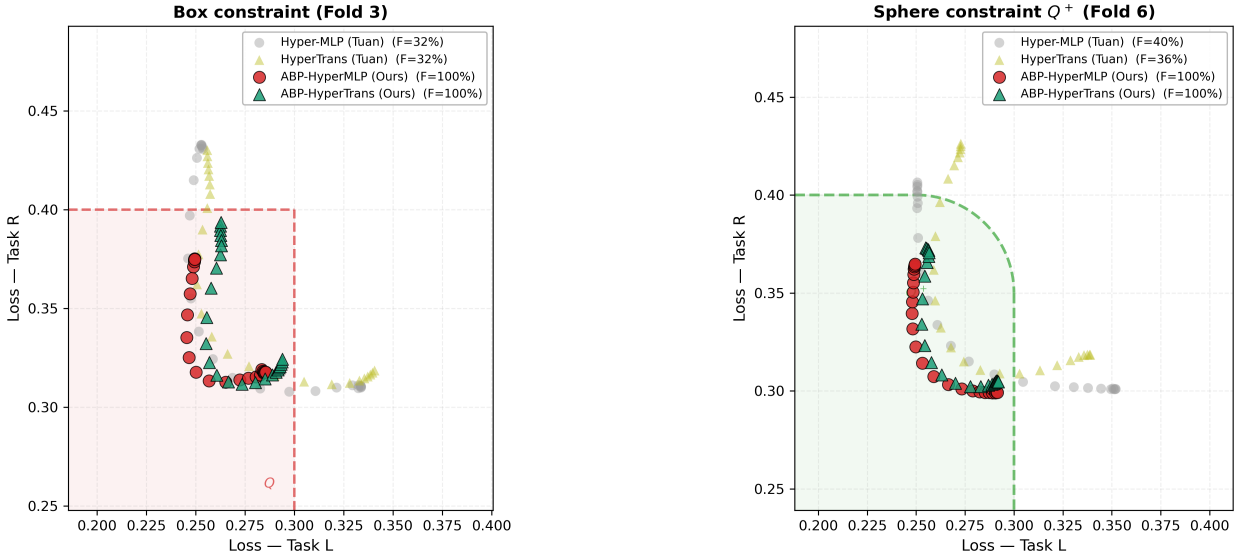


Figure 8: Multi-MNIST: Pareto fronts of all four methods under Box (left) and Sphere (right) constraints for a representative fold. Shaded regions: constraint set Q / Q^+ ; legend shows ray-level feasibility.

Multi-Fashion

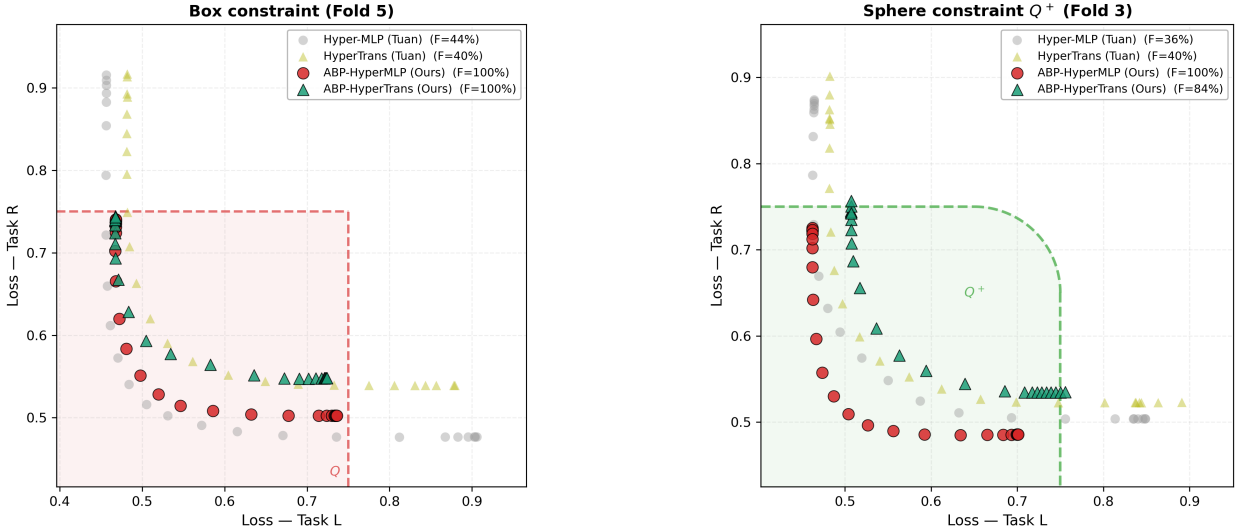


Figure 9: Multi-Fashion: Pareto fronts of all four methods. Layout as in Fig. 8.

no adaptive β . **Hard-Switch** uses pure \mathcal{L}_Q in Phase 1 ($\epsilon = 0$) and pure \mathcal{L}_{obj} in Phase 2 ($\beta = 0$), creating an abrupt loss discontinuity at the transition.

A clear ranking emerges (Table 9): Full \approx No-Phase1 \gg No-Adaptive- β $>$ Single-Phase \gg Hard-Switch. The Full strategy achieves the highest EFHV (2.550) and feasibility (93.2%). Hard-Switch suffers the most ($\pi = 62.7\%$, EFHV = 1.740), driven by catastrophic feasibility collapse on Multi-Fashion ($\pi = 40\%$) and Fashion+MNIST ($\pi = 48\%$), confirming that an abrupt loss discontinuity prevents effective constraint enforcement. No-Phase1 is

Fashion+MNIST

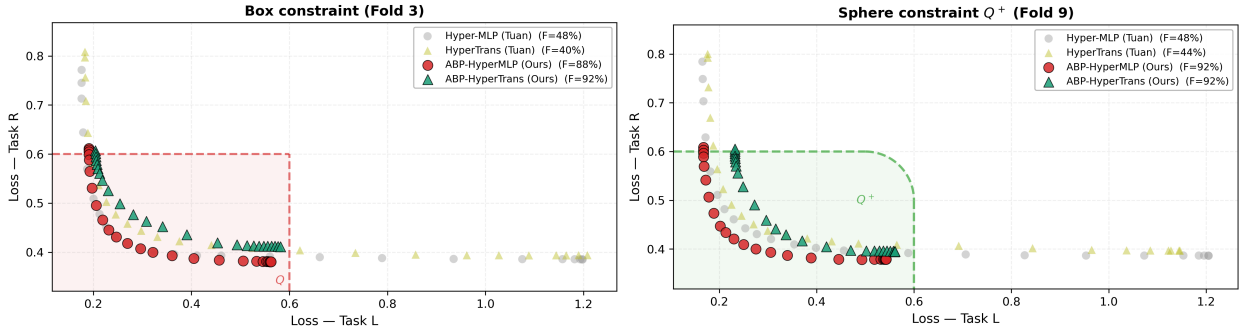


Figure 10: Fashion+MNIST: Pareto fronts of all four methods. Layout as in Fig. 8.

Table 9

Ablation study: mean across three MTL datasets (ABP-HyperMLP, Box constraint, 10-fold CV). **Bold**: best per metric.

Variant	π (%) (\uparrow)	HV (\uparrow)	EFHV (\uparrow)
Full (proposed)	93.2	2.736	2.550
No-Phase1	92.5	2.736	2.540
No-Adaptive- β	90.5	2.693	2.424
Single-Phase	82.9	2.684	2.205
Hard-Switch	62.7	2.677	1.740

close to Full in aggregate (EFHV = 2.540, -0.4%), but exhibits lower robustness: on Multi-Fashion its feasibility drops to 88.8% versus 94.0% for Full, indicating that the warm-up phase provides a more reliable starting point on harder constraints. Removing adaptive penalty adjustment (No-Adaptive- β) reduces EFHV by 4.9%, while the naive Single-Phase baseline loses 13.5%, confirming the value of both the phase structure and the dynamic penalty schedule.

8. Conclusion

We have proposed the Adaptive Balanced Penalty (ABP) algorithm for the Bi-Level Scalarized Split Problem (BSSP) and proved that the full sequence of iterates converges to an optimal solution under standard convexity, step-size, and zero-gap assumptions. The ABP penalty structure is translated into a two-phase, feasibility-first training strategy for hypernetworks (ABP-HyperMLP, ABP-HyperTrans), and evaluated through a dedicated metric—the Expected Feasible Hypervolume (EFHV)—that jointly captures solution quality and constraint satisfaction.

Summary of results. On five multi-objective benchmarks (Section 6), the ABP solver closely approximates the ground-truth constrained Pareto front, and ABP-HyperTrans preserves this accuracy at real-time inference cost. On three multi-task learning datasets (Section 7), ABP-HyperNet raises feasibility from the baselines' 36–49% to 87–100%, yielding up to $2.3\times$ higher EFHV while incurring at most ≈ 0.02 HV cost relative to the unconstrained upper bound.

The convex surrogate technique. The linearized half-space surrogate δ_k (Section 4.2.1) converts the non-convex image-feasibility function G into a global subgradient inequality at each iteration. This technique is applicable to any split feasibility problem involving a convex mapping and a convex target set, and may be of independent interest.

Limitations and future work. The zero-gap Assumption (A7) is a structural condition on the interplay between the Pareto front and the target region Q^+ ; developing an algorithm that achieves exact convergence without this condition—for instance through a dynamically updated lower bound or a Lagrangian dual approach—is an important

open problem. Extending the convergence analysis to the stochastic, non-convex regime and scaling to many-objective problems ($m \geq 4$) are additional directions for future work.

A. Full proofs for Section 4

This appendix provides complete proofs for all results stated in Section 4. Results are organized following the logical dependency order of the proof chain. All lemma and theorem numbers are identical to those in the main body.

A.1. Technical lemmas (Lemmas 4.1–4.8)

Lemma 4.1 (restated). Under (A2), H is convex and C^1 with $\nabla H(x) = x - P_C(x)$.

Role: Used in Lemma 4.7 and Lemma 4.9.

PROOF. H is the infimal convolution of $\frac{1}{2}\|\cdot\|^2$ with the indicator of C , hence convex (Bauschke and Combettes, 2017, Proposition 12.9). Differentiability and the gradient formula follow from Danskin's theorem (Bertsekas, 1999, Proposition B.22).

Lemma 4.2 (restated). Under (A1) and (A3), φ is convex and $w^k \in \partial\varphi(x^k)$ for every choice of i^* in (14).

Role: Used in Lemma 4.6.

PROOF. $\varphi = \max_i r_i(f_i - z_i^*)$ is convex as a pointwise maximum of convex functions. Let $\phi_{i^*} := r_{i^*}(f_{i^*} - z_{i^*}^*)$; then $\phi_{i^*}(x^k) = \varphi(x^k)$ and $\phi_{i^*} \leq \varphi$. Convexity of ϕ_{i^*} gives $\varphi(y) \geq \phi_{i^*}(y) \geq \varphi(x^k) + \langle w^k, y - x^k \rangle$ for all y , confirming $w^k \in \partial\varphi(x^k)$.

Lemma 4.3 (restated). $Q^+ \subseteq Q_k^+$ for every k .

Role: Used in Lemma 4.8 via $\delta_k \leq G$ pointwise.

PROOF. The projection characterization (Bauschke and Combettes, 2017, Theorem 3.14) gives $\langle \rho^k, w - p^k \rangle \leq 0$ for every $w \in Q^+$.

Lemma 4.4 (restated). Under (A1) and (A3), δ_k is convex.

Role: Used in Lemma 4.8 to apply the gradient inequality for the convex function δ_k .

PROOF. Trivial when $\rho^k = 0$. For $\rho^k \neq 0$, set $h_k(x) := \sum_i \rho_i^k f_i(x)$, which is convex since each f_i is convex and $\rho_i^k \geq 0$ (Corollary 2.4). Then $\delta_k(x) = \psi(h_k(x) - \langle \rho^k, p^k \rangle) / (2\|\rho^k\|^2)$ where $\psi(t) := [t]_+^2$ is convex and nondecreasing. Convexity of δ_k follows from the composition rule (Hiriart-Urruty and Lemaréchal, 2004, Proposition 1.2.4).

Lemma 4.5 (restated). For every k : $\delta_k(x^k) = G_k$, and $\nabla\delta_k(x^k) = v^k$ (with $v^k = 0$ when $\rho^k = 0$).

Role: Used in Lemma 4.8 to identify $\nabla\delta_k(x^k) = v^k$.

PROOF. When $\rho^k = 0$: $G_k = \delta_k(x^k) = 0$ and $v^k = 0$. When $\rho^k \neq 0$: since $\langle \rho^k, F(x^k) - p^k \rangle = \|\rho^k\|^2 > 0$, the $[\cdot]_+$ in (17) is active and $\delta_k(x^k) = \|\rho^k\|^2 / 2 = G_k$. Setting $\Psi(x) := \langle \rho^k, F(x) - p^k \rangle$, we have $\Psi(x^k) > 0$ so $\delta_k = \Psi^2 / (2\|\rho^k\|^2)$ is C^1 near x^k , and the chain rule gives $\nabla\delta_k(x^k) = \Psi(x^k) J_F(x^k)^T \rho^k / \|\rho^k\|^2 = J_F(x^k)^T \rho^k = v^k$.

Lemma 4.6 (restated). Under (A1), (A3), (A7): $\langle w^k, x^k - x^* \rangle \geq \Delta_k$ for all k and $x^* \in \Omega$.

Role: Used in Lemma 4.9 (case $\Delta_k \geq 0$).

PROOF. From $w^k \in \partial\varphi(x^k)$: $\varphi(x^*) \geq \varphi(x^k) + \langle w^k, x^* - x^k \rangle$. Using $\varphi(x^*) = \varphi^* = \varphi_{\text{lb}}$ (by (A7)) and rearranging gives $\langle w^k, x^k - x^* \rangle \geq \Delta_k$.

Lemma 4.7 (restated). Under (A2): $\langle z^k, x^k - x^* \rangle \geq H_k \geq 0$ for all k and $x^* \in \Omega$.

Role: Used in Lemma 4.9 (both cases).

PROOF. Convexity of H and $H(x^*) = 0$ give $0 \geq H_k + \langle z^k, x^* - x^k \rangle$; rearranging yields the result.

Lemma 4.8 (restated). Under (A1)–(A3), v^k satisfies a global subgradient inequality for G : $G(y) \geq G_k + \langle v^k, y - x^k \rangle$ for all $y \in \mathbb{R}^n$, $k \geq 0$.

Role: Used in Lemma 4.9 (both cases).

PROOF. When $\rho^k = 0$: $G_k = v^k = 0$ and (18) holds trivially. When $\rho^k \neq 0$: Lemma 4.3 gives $\delta_k \leq G$ pointwise. Using the gradient inequality for the convex function δ_k (Lemmas 4.4 and 4.5): $G(y) \geq \delta_k(y) \geq G_k + \langle v^k, y - x^k \rangle$. Setting $y = x^* \in S$ gives $\langle v^k, x^k - x^* \rangle \geq G_k$.

A.2. Lyapunov analysis (Lemma 4.9, Proposition 4.11, Lemma 4.12)

Lemma 4.9 (*Lyapunov inequality, restated*). Under Assumption 1, for every $x^* \in \Omega$ and $k \geq 0$, $\|x^{k+1} - x^*\|^2 \leq \|x^k - x^*\|^2 - (2\lambda_k/\eta_k)\Phi_k + \lambda_k^2$.

Role: Central recursive inequality; used in Lemmas 4.13 and 4.19.

PROOF. Expanding $\|x^{k+1} - x^*\|^2$ using $x^{k+1} = x^k - (\lambda_k/\eta_k)d^k$ and bounding $\lambda_k^2\|d^k\|^2/\eta_k^2 \leq \lambda_k^2$ (since $\eta_k \geq \|d^k\|$), it suffices to show $\langle d^k, x^k - x^* \rangle \geq \Phi_k$. By (15) and Lemmas 4.7–4.8:

$$\langle d^k, x^k - x^* \rangle \geq \alpha_k \mathbf{1}_{\{\Delta_k \geq 0\}} \langle w^k, x^k - x^* \rangle + \beta_k H_k + \gamma_k G_k.$$

If $\Delta_k \geq 0$: Lemma 4.6 gives the first term $\geq \alpha_k \Delta_k = \alpha_k \Delta_k^+$, so $\langle d^k, x^k - x^* \rangle \geq \Phi_k$. If $\Delta_k < 0$: $\Delta_k^+ = 0$ and the indicator vanishes, so $\langle d^k, x^k - x^* \rangle \geq \beta_k H_k + \gamma_k G_k = \Phi_k$.

Proposition 4.11 (*Quasi-Fejér property, restated*). Under Assumption 1, the sequence $\{\|x^k - x^*\|^2\}$ converges for every $x^* \in \Omega$; in particular, $\{x^k\}$ is bounded.

Role: Establishes boundedness of $\{x^k\}$; used in Lemma 4.12 and Proposition 4.16.

PROOF. Drop the nonpositive term in (20) to get $\|x^{k+1} - x^*\|^2 \leq \|x^k - x^*\|^2 + \lambda_k^2$. Apply Lemma 4.10 with $b_k := \lambda_k^2$; summability holds by (A5).

Lemma 4.12 (*restated*). Under Assumption 1, $\|d^k\| \leq \bar{M} < \infty$ for all k , and $\mu \leq \eta_k \leq \bar{\eta} := \max(\mu, \bar{M})$.

Role: Bounds $\|d^k\|$ and η_k ; used in Lemmas 4.13 and 4.20.

PROOF. By Proposition 4.11, $\{x^k\}$ lies in a compact ball $K = \bar{B}(x^*, R)$. Nonexpansiveness of P_C gives $\|z^k\| \leq 2R$. Continuity of each ∇f_i on K bounds $\|w^k\| \leq M_w$. Continuity of \mathcal{F} and $J_{\mathcal{F}}$ on K gives $\|\rho^k\| \leq M_\rho$ and $\|J_{\mathcal{F}}(x^k)\|_{\text{op}} \leq M_J$, hence $\|v^k\| \leq M_J M_\rho$. By (A6): $\|d^k\| \leq \bar{\alpha} M_w + 2\bar{\beta} R + \bar{\gamma} M_J M_\rho =: \bar{M}$.

A.3. Global convergence: proof of Theorem 4.17

Lemma 4.13 (*restated*). $\sum_{k=0}^{\infty} \lambda_k \Phi_k < \infty$.

PROOF. Sum (20) from 0 to $N - 1$ and drop the nonnegative term $\|x^N - x^*\|^2$: $\sum_{k=0}^{N-1} (2\lambda_k/\eta_k)\Phi_k \leq \|x^0 - x^*\|^2 + \sum_{k=0}^{N-1} \lambda_k^2$. Since $\eta_k \leq \bar{\eta}$ (Lemma 4.12), letting $N \rightarrow \infty$ gives the result using (A5).

Lemma 4.14 (*restated*). $\liminf_{k \rightarrow \infty} \Phi_k = 0$.

PROOF. If $\Phi_k \geq \delta > 0$ for all $k \geq k_0$, then $\sum_{k \geq k_0} \lambda_k \Phi_k \geq \delta \sum_{k \geq k_0} \lambda_k = \infty$ by (A5), contradicting Lemma 4.13.

Proposition 4.15 (*restated*). There exists a subsequence $\{k_j\}$ with $\Delta_{k_j}^+ \rightarrow 0$, $H_{k_j} \rightarrow 0$, $G_{k_j} \rightarrow 0$, and $\Delta_{k_j} \rightarrow 0$.

PROOF. Extract $\{k_j\}$ with $\Phi_{k_j} \rightarrow 0$ (Lemma 4.14).

Step 1. $\Phi_{k_j} \geq \underline{\beta} H_{k_j} + \underline{\gamma} G_{k_j}$, so $H_{k_j} \rightarrow 0$ and $G_{k_j} \rightarrow 0$. Then $\alpha_{k_j} \Delta_{k_j}^+ = \Phi_{k_j} - \beta_{k_j} H_{k_j} - \gamma_{k_j} G_{k_j} \rightarrow 0$, and $\alpha_{k_j} \geq \underline{\alpha} > 0$ gives $\Delta_{k_j}^+ \rightarrow 0$.

Step 2. We show $\liminf_j \Delta_{k_j} \geq 0$. Suppose not; extract a further subsequence with $x^{k_j} \rightarrow \hat{x}$ and $\Delta_{k_j} \rightarrow \ell_0 < 0$. From $H_{k_j} \rightarrow 0$ and closedness of C : $\hat{x} \in C$. From $G_{k_j} \rightarrow 0$, continuity of \mathcal{F} , and closedness of \mathcal{Q}^+ : $\mathcal{F}(\hat{x}) \in \mathcal{Q}^+$, so $\hat{x} \in S$. By continuity of φ and assumption (A7): $\varphi(\hat{x}) = \ell_0 + \varphi_{\text{lb}} = \ell_0 + \varphi^* < \varphi^*$, contradicting $\hat{x} \in S$. Hence $\Delta_{k_j} \rightarrow 0$.

Proposition 4.16 (*restated*). There exist a subsequence $\{k_j\}$ and $x^\infty \in \Omega$ with $x^{k_j} \rightarrow x^\infty$.

PROOF. Take $\{k_j\}$ from Proposition 4.15; extract a convergent sub-subsequence $x^{k_j} \rightarrow x^\infty$ using boundedness (Proposition 4.11). Step 2 of Proposition 4.15 (with $\ell_0 = 0$) shows $x^\infty \in S$, and $\Delta_{k_j} \rightarrow 0$ with continuity of φ gives $\varphi(x^\infty) = \varphi_{\text{lb}} = \varphi^*$, so $x^\infty \in \Omega$.

Theorem 4.17 (*Global convergence, restated*). Under Assumption 1, $\{x^k\}$ generated by the ABP algorithm (Algorithm 1) converges to some $x^\infty \in \Omega$.

PROOF. Let x^∞ be as in Proposition 4.16. By Proposition 4.11 (applied with $x^* := x^\infty$, valid for every $x^* \in \Omega$), the sequence $a_k := \|x^k - x^\infty\|^2$ converges to some $a^* \geq 0$. Along $\{k_j\}$: $a_{k_j} \rightarrow 0$, so $a^* = 0$ and $x^k \rightarrow x^\infty$.

A.4. Approximate convergence: proof of Theorem 4.22

Lemma 4.18 (Modified optimality inner product, restated). Let $x^* \in \Omega$. Under (A1), (A3), (A7'): $\langle w^k, x^k - x^* \rangle \geq \Delta_k - \sigma$ for all $k \geq 0$.

PROOF. The subgradient inequality $w^k \in \partial\varphi(x^k)$ gives $\varphi(x^*) \geq \varphi(x^k) + \langle w^k, x^* - x^k \rangle$, so

$$\langle w^k, x^k - x^* \rangle \geq \varphi(x^k) - \varphi(x^*) = \Delta_k + \varphi_{\text{lb}} - \varphi^* = \Delta_k - \sigma.$$

Lemma 4.19 (Modified Lyapunov inequality, restated). Under (A1)–(A6), (A7'), (A8), for every $x^* \in \Omega$, $\|x^{k+1} - x^*\|^2 \leq \|x^k - x^*\|^2 - (2\lambda_k/\eta_k)\Phi_k + (2\bar{\alpha}\sigma/\mu)\lambda_k + \lambda_k^2$.

PROOF. Expanding $x^{k+1} = x^k - (\lambda_k/\eta_k)d^k$:

$$\|x^{k+1} - x^*\|^2 = \|x^k - x^*\|^2 - \frac{2\lambda_k}{\eta_k} \langle d^k, x^k - x^* \rangle + \frac{\lambda_k^2}{\eta_k^2} \|d^k\|^2.$$

Since $\eta_k \geq \|d^k\|$, the last term satisfies $\lambda_k^2 \|d^k\|^2 / \eta_k^2 \leq \lambda_k^2$. It remains to bound $\langle d^k, x^k - x^* \rangle$ from below.

Case $\Delta_k < 0$ (indicator = 0): $d^k = \beta_k z^k + \gamma_k v^k$, so by Lemmas 4.7 and 4.8,

$$\langle d^k, x^k - x^* \rangle \geq \beta_k H_k + \gamma_k G_k = \Phi_k \geq \Phi_k - \bar{\alpha}\sigma.$$

Case $\Delta_k \geq 0$ (indicator = 1): Using Lemma 4.18 and Lemmas 4.7 and 4.8:

$$\begin{aligned} \langle d^k, x^k - x^* \rangle &\geq \alpha_k(\Delta_k - \sigma) + \beta_k H_k + \gamma_k G_k \\ &= \alpha_k \Delta_k^+ + \beta_k H_k + \gamma_k G_k - \alpha_k \sigma = \Phi_k - \alpha_k \sigma \geq \Phi_k - \bar{\alpha}\sigma. \end{aligned}$$

In both cases $\langle d^k, x^k - x^* \rangle \geq \Phi_k - \bar{\alpha}\sigma$. Using $\eta_k \geq \mu$:

$$-\frac{2\lambda_k}{\eta_k} \langle d^k, x^k - x^* \rangle \leq -\frac{2\lambda_k}{\eta_k} \Phi_k + \frac{2\bar{\alpha}\sigma}{\eta_k} \lambda_k \leq -\frac{2\lambda_k}{\eta_k} \Phi_k + \frac{2\bar{\alpha}\sigma}{\mu} \lambda_k.$$

The drift term and its consequences. Compared with the Lyapunov inequality (20), the only new term is the drift $(2\bar{\alpha}\sigma/\mu)\lambda_k$. When $\sigma = 0$ it vanishes and the original recursion is recovered. When $\sigma > 0$, the partial sum $(2\bar{\alpha}\sigma/\mu)\Lambda_N \rightarrow \infty$ as $N \rightarrow \infty$ (since $\sum \lambda_k = \infty$). Consequently the Robbins–Siegmund lemma cannot be applied to $\|x^k - x^*\|^2$, and the sequence may fail to be bounded; hence Assumption (A8) is necessary for the analysis that follows.

A.4.1. Ergodic and simultaneous approximate bounds

Lemma 4.20 (Ergodic bound, restated). Under (A1)–(A6), (A7'), (A8), define $C_* := \bar{\alpha}\bar{\eta}/\mu$ and $\Lambda_N := \sum_{k=0}^N \lambda_k$. Then $\limsup_{N \rightarrow \infty} \Lambda_N^{-1} \sum_{k=0}^N \lambda_k \Phi_k \leq C_* \varepsilon_0$ and $\liminf_{k \rightarrow \infty} \Phi_k \leq C_* \varepsilon_0$.

PROOF. Fix any $x^* \in \Omega$ and sum (22) from $k = 0$ to $k = N$:

$$2 \sum_{k=0}^N \frac{\lambda_k}{\eta_k} \Phi_k \leq \|x^0 - x^*\|^2 - \|x^{N+1} - x^*\|^2 + \frac{2\bar{\alpha}\sigma}{\mu} \Lambda_N + \sum_{k=0}^N \lambda_k^2. \quad (40)$$

Since $\eta_k \leq \bar{\eta}$ for all k , we have $\lambda_k/\eta_k \geq \lambda_k/\bar{\eta}$, so

$$\frac{2}{\bar{\eta}} \sum_{k=0}^N \lambda_k \Phi_k \leq 2 \sum_{k=0}^N \frac{\lambda_k}{\eta_k} \Phi_k.$$

Combining with (40) and dropping $-\|x^{N+1} - x^*\|^2 \leq 0$:

$$\frac{2}{\bar{\eta}} \sum_{k=0}^N \lambda_k \Phi_k \leq \|x^0 - x^*\|^2 + \frac{2\bar{\alpha}\sigma}{\mu} \Lambda_N + \sum_{k=0}^N \lambda_k^2.$$

Dividing by $\Lambda_N > 0$ and taking $N \rightarrow \infty$: the term $(\|x^0 - x^*\|^2 + \sum_{k=0}^{\infty} \lambda_k^2) / \Lambda_N \rightarrow 0$ (finite numerator, by (A5); $\Lambda_N \rightarrow \infty$, by (A5)). Using $\sigma \leq \varepsilon_0$ yields (23) after multiplying by $\bar{\eta}/2$.

For (24): if $\Phi_k > C_* \varepsilon_0 + \delta$ for all $k \geq k_0$ and some $\delta > 0$, then $\Lambda_N^{-1} \sum_{k=0}^N \lambda_k \Phi_k > C_* \varepsilon_0 + \delta - O(1/\Lambda_N)$, and taking $N \rightarrow \infty$ gives $\limsup > C_* \varepsilon_0$, contradicting (23).

Proposition 4.21 (*Approximate simultaneous bounds, restated*). Under (A1)–(A6), (A7'), (A8), there exist a subsequence $\{k_j\}$ and $\ell_* \in [0, C_*\varepsilon_0]$ with $\Phi_{k_j} \rightarrow \ell_*$ and $H_{k_j} \leq \Phi_{k_j}/\underline{\beta}$, $G_{k_j} \leq \Phi_{k_j}/\underline{\gamma}$, $\Delta_{k_j}^+ \leq \Phi_{k_j}/\underline{\alpha}$.

PROOF. By Lemma 4.20, extract a subsequence $\{k_j\}$ with $\Phi_{k_j} \rightarrow \ell_* \leq C_*\varepsilon_0$. Since each summand of Φ_k is nonnegative:

$$\underline{\alpha} \Delta_{k_j}^+ \leq \Phi_{k_j}, \quad \underline{\beta} H_{k_j} \leq \Phi_{k_j}, \quad \underline{\gamma} G_{k_j} \leq \Phi_{k_j}.$$

Dividing by the respective lower bounds and letting $j \rightarrow \infty$ yields (25)–(27). When $\varepsilon_0 = 0$, $\ell_* = 0$ and each upper bound is 0; since each term is also nonnegative, all three sequences converge to 0.

Remark. Equations (25)–(26) provide upper bounds on H_{k_j} and G_{k_j} whose limits equal $\ell_*/\underline{\beta}$ and $\ell_*/\underline{\gamma}$ respectively; these limits are zero only when $\varepsilon_0 = 0$. The cluster-point bounds in Theorem 4.22 are consequently stated as inequalities \leq , not as equalities, reflecting the fact that continuity of H and G transfers the upper bound—not an exact limit—to any cluster point \hat{x} .

A.4.2. Main approximate convergence theorem

Theorem 4.22 (*Approximate convergence, restated*). Under (A1)–(A6), (A7'), (A8), let $C_* = \bar{\alpha}\bar{\eta}/\mu$. Every cluster point \hat{x} satisfies approximate feasibility in C , approximate split feasibility, and approximate optimality bounds that vanish when $\varepsilon_0 = 0$.

PROOF. By (A8) and the Bolzano–Weierstrass theorem, extract a further subsequence (still denoted $\{k_j\}$) with $x^{k_j} \rightarrow \hat{x}$.

Proofs of (i) and (ii). The function $H(x) = \frac{1}{2}\text{dist}^2(x, C)$ is continuous (Lemma 4.1). The function $G(x) = \frac{1}{2}\text{dist}^2(\mathcal{F}(x), Q^+)$ is continuous by continuity of \mathcal{F} (A1) and continuity of the projection onto the closed convex set Q^+ . Using continuity of H and the bound (25):

$$H(\hat{x}) = \lim_{j \rightarrow \infty} H(x^{k_j}) = \lim_{j \rightarrow \infty} H_{k_j} \leq \lim_{j \rightarrow \infty} \frac{\Phi_{k_j}}{\underline{\beta}} = \frac{\ell_*}{\underline{\beta}} \leq \frac{C_*\varepsilon_0}{\underline{\beta}}.$$

The distance bound $\text{dist}(\hat{x}, C) \leq \sqrt{2C_*\varepsilon_0/\underline{\beta}}$ follows by taking square roots and multiplying by $\sqrt{2}$. The argument for $G(\hat{x})$ is identical, using (26).

Proof of (iii). Since φ is continuous (A1), (A3):

$$\varphi(\hat{x}) = \lim_{j \rightarrow \infty} \varphi(x^{k_j}) = \lim_{j \rightarrow \infty} (\Delta_{k_j} + \varphi_{\text{lb}}).$$

From (27), $\Delta_{k_j} \leq \Delta_{k_j}^+ \leq \ell_*/\underline{\alpha} + o(1)$, so taking the limit:

$$\varphi(\hat{x}) \leq \varphi_{\text{lb}} + \frac{\ell_*}{\underline{\alpha}} \leq \varphi^* + \frac{\ell_*}{\underline{\alpha}} \leq \varphi^* + \frac{C_*\varepsilon_0}{\underline{\alpha}}.$$

Exact convergence when $\varepsilon_0 = 0$. If $\varepsilon_0 = 0$ then $\ell_* = 0$ (Proposition 4.21). From (i): $H(\hat{x}) = 0$, so $\text{dist}(\hat{x}, C) = 0$ and closedness of C gives $\hat{x} \in C$. From (ii): $G(\hat{x}) = 0$, so $\text{dist}(\mathcal{F}(\hat{x}), Q^+) = 0$ and closedness of Q^+ gives $\mathcal{F}(\hat{x}) \in Q^+$. Hence $\hat{x} \in S$. From (iii): $\varphi(\hat{x}) \leq \varphi^*$. Combined with $\hat{x} \in S$ and the definition $\varphi^* = \inf_{x \in S} \varphi(x)$: $\varphi(\hat{x}) = \varphi^*$, so $\hat{x} \in \Omega$.

B. Constraint geometry visualization

This appendix complements the main-body results (Tables 6–8) with two additions: (i) the unconstrained ABP baseline ($Q = \mathbb{R}^m$, denoted “None”), which was not reported in Section 7.2, and (ii) per-architecture Pareto front visualizations under all three constraint settings. Rather than repeating the absolute HV, π , and EFHV values already given in Tables 6–8, Table 10 reports the *cost of constraint enforcement*: the unconstrained HV serves as the upper bound, and $\Delta\text{HV} = \text{HV}_{\text{None}} - \text{HV}_Q$ quantifies how much front coverage is sacrificed to achieve feasibility rate π .

Table 10

Cost of constraint enforcement for ABP-HyperMLP and ABP-HyperTrans on each dataset. HV_{None} : unconstrained hypervolume (upper bound); ΔHV : HV loss due to constraint (> 0 means coverage reduced; ≤ 0 means no loss); π : feasibility rate achieved by the constrained model (from Tables 6–8). All values are means over 10-fold CV with reference point $(2, 2)$.

Dataset	Architecture	HV_{None}	Constr.	ΔHV (\downarrow)	π (%) (\uparrow)
Multi-MNIST	ABP-HyperMLP	2.979	Box	0.021	100.0
			Sphere	0.011	100.0
	ABP-HyperTrans	2.970	Box	0.011	92.5
			Sphere	0.015	99.5
Multi-Fashion	ABP-HyperMLP	2.337	Box	0.021	94.9
			Sphere	0.015	100.0
	ABP-HyperTrans	2.201	Box	0.005	90.3
			Sphere	0.006	89.1
Fashion+MNIST	ABP-HyperMLP	2.928	Box	0.000	87.4
			Sphere	-0.007	88.6
	ABP-HyperTrans	2.847	Box	0.003	90.9
			Sphere	-0.020	91.4

Analysis. Table 10 reveals that the HV cost of constraint enforcement is consistently small. Across all 12 (dataset, architecture, constraint) combinations, the largest positive ΔHV is only 0.021, corresponding to a relative loss of less than 1%. On Fashion+MNIST, ΔHV is zero or slightly negative, indicating that the constraint penalty can act as an implicit regularizer that marginally *improves* front quality. Comparing constraint geometries, Sphere constraints generally achieve higher feasibility than Box for the same architecture (e.g., ABP-HyperTrans on Multi-MNIST: $\pi = 99.5\%$ vs. 92.5% ; ABP-HyperMLP on Multi-Fashion: $\pi = 100.0\%$ vs. 94.9%), which is consistent with the smoother gradient landscape of the ball projection $P_{B(c,R)}$ compared to the axis-aligned Box projection. The only exception is Fashion+MNIST, where both constraint types yield similar π values (87–91%), suggesting that the asymmetric task structure—rather than constraint geometry—is the dominant factor affecting feasibility.

Qualitative visualization. Figures 11–16 show the Pareto fronts produced by each ABP variant under all three constraint settings for a representative fold of each dataset. In each panel, the unconstrained solutions (None, blue) trace the full Pareto curve, while the Box (red) and Sphere (green) solutions retract into the feasible region—indicated by dashed boundaries and shading—without collapsing diversity along the front. The visual patterns are consistent with the quantitative findings in Table 10: front coverage is largely preserved while solutions are redirected into the target region Q .

C. Supplementary experimental details

C.1. Verification of Assumptions (A7)–(A8) for CVX1 and CVX2

For CVX1 and CVX2 the decision set C is a compact box, so Assumption (A8) holds automatically for any initialization $x^0 \in C$. To assess the zero-gap condition, we compute

$$\varphi_{\text{lb}} = \min_{x \in C} \varphi(x; \mathbf{r}) \quad \text{and} \quad \varphi^* = \min_{x \in S} \varphi(x; \mathbf{r})$$

via SLSQP with analytical Jacobian for each of the 50 preference rays \mathbf{r} . The resulting gap $\sigma(\mathbf{r}) := \varphi^*(\mathbf{r}) - \varphi_{\text{lb}}(\mathbf{r})$ is reported in Table 11. For rays where $\sigma = 0$, the zero-gap condition (A7) holds exactly and Theorem 4.17 guarantees full-sequence convergence. For rays where $\sigma > 0$, Theorem 4.22 applies with $\varepsilon_0 = \sigma$.

C.2. Effect of the number of preference rays

Table 12 reports MED (\downarrow) and HV (\uparrow) on CVX2 for ABP-HyperMLP and ABP-HyperTrans as the number of preference rays varies from 10 to 100.

Table 11

Optimality gap $\sigma = \varphi^* - \varphi_{lb}$ over 50 preference rays. Full-sequence convergence (Theorem 4.17) applies on rays with $\sigma = 0$; approximate convergence (Theorem 4.22) applies otherwise.

Problem	σ_{\min}	σ_{\max}	σ_{mean}	Rays with $\sigma = 0$
CVX1	0.0000	0.0806	0.0090	39/50
CVX2	0.0000	0.0134	0.0005	44/50

Table 12

Effect of the number of preference rays on MED (\downarrow) and HV (\uparrow) for CVX2, reported for a single representative run (not multi-seed averages; cf. Table 4 for mean \pm std over 10 seeds at 50 rays). Best result per metric and architecture is **bold**.

Method	10 rays		20 rays		50 rays		100 rays	
	MED	HV	MED	HV	MED	HV	MED	HV
ABP-HyperMLP	0.00830	1.6298	0.00535	1.6690	0.00443	1.6886	0.00384	1.6910
ABP-HyperTrans	0.00461	1.6392	0.00322	1.6788	0.00242	1.6937	0.00212	1.6982

Both MED and HV improve monotonically with the number of rays: ABP-HyperTrans’s MED drops by 47% from 10 to 50 rays (0.00461 \rightarrow 0.00242) and by a further 12% from 50 to 100 rays (0.00242 \rightarrow 0.00212). Visually, Fig. 17 confirms that denser ray sampling yields a more complete coverage of the constrained Pareto front inside Q^+ . For consistency with the baseline of (Tuan et al., 2024b), all MOP experiments in this paper use 50 rays.

C.3. Hyperparameter sensitivity

The two-phase training strategy introduces four key hyperparameters that govern the balance between feasibility enforcement and Chebyshev optimization. We conduct a sensitivity study on Multi-MNIST (Hyper-MLP, Box constraint $\mathbf{b} = (0.30, 0.40)$, 300 epochs), sweeping each hyperparameter across five values while keeping the remaining ones at their defaults. Each configuration is evaluated over five independent seeds; Figure 18 reports mean Hypervolume (HV) and feasibility rate.

Phase-1 objective weight ε . During Phase 1 the loss is $\mathcal{L}_Q + \varepsilon \mathcal{L}_{\text{obj}}$. Setting $\varepsilon = 0$ yields 100% feasibility but the highest HV variance, because the hypernetwork does not learn the preference-to-solution mapping during warm-up and must acquire it from scratch in Phase 2. Conversely, $\varepsilon = 0.50$ overweights the Chebyshev term, extending Phase 1 to 70 of 80 budgeted epochs and dropping feasibility to 86%. The range $\varepsilon \in [0.01, 0.10]$ balances diversity preservation with rapid feasibility convergence; we adopt $\varepsilon = 0.10$ as the default.

Penalty growth factor ρ . In Phase 2 the constraint coefficient β is multiplied by ρ (resp. $\rho^{-1} \approx 0.98$) whenever feasibility drops below (resp. exceeds) the target. With $\rho = 1.00$ (constant β) feasibility falls to 84% because the restoring force cannot compensate for the optimality-driven drift. Increasing ρ to 1.05–1.10 lifts feasibility above 94% while improving HV (from 2.970 to 2.977). At $\rho = 1.20$ HV reaches 2.981 but feasibility variance increases, indicating occasional over-penalization that flattens the Pareto front approximation in some seeds. The default $\rho = 1.05$ offers a robust trade-off.

Penalty cap β_{\max} . The multiplicative cap limits how large β can grow. For $\beta_{\max} = 2$ the ceiling is reached too early and feasibility drops to 93%; for $\beta_{\max} \geq 10$ the cap is rarely activated and performance stabilizes (HV \approx 2.974–2.979, feasibility \approx 94%). We set $\beta_{\max} = 10$ as a conservative default.

Initial penalty β_0 . When Phase 2 begins, the penalty coefficient is initialized to β_0 . Starting with a weak penalty ($\beta_0 \leq 0.5$) causes a transient feasibility dip as rays drift outside Q before the adaptive schedule compensates, reducing HV to \approx 2.962. Values $\beta_0 \geq 1.0$ prevent this drift; $\beta_0 = 5.0$ yields the best feasibility (97.6%) at the cost of slightly reduced solution diversity. The default $\beta_0 = 1.0$ balances these effects.

Overall, the method is robust across the tested ranges: HV remains within [2.961, 2.985] and feasibility stays above 84% in all 20 configurations. The most sensitive parameters are the Phase-1 weight ε and the growth factor ρ , both of which directly govern the balance between optimality and constraint enforcement in their respective phases.

Multi-MNIST — Hyper-MLP Model

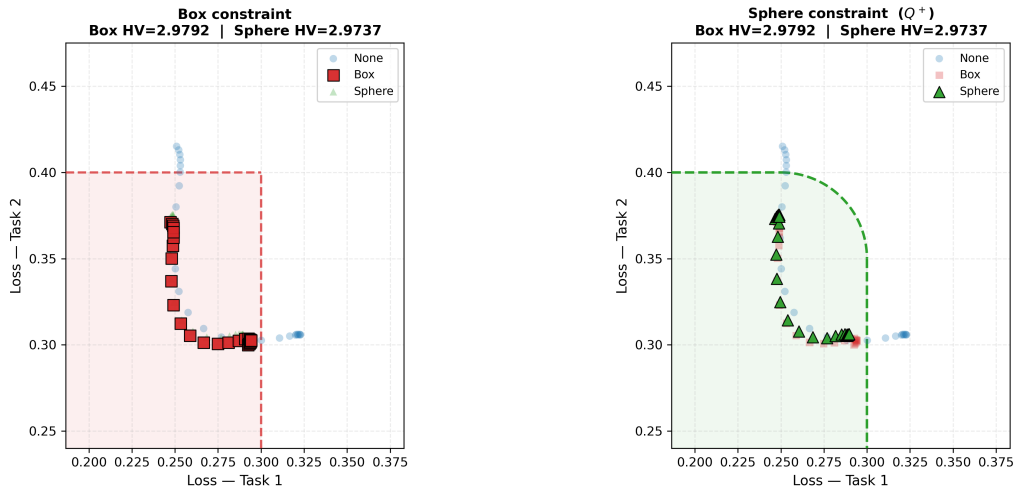


Figure 11: Multi-MNIST, ABP-HyperMLP: Pareto front under None (blue), Box (red), and Sphere (green) constraints. Dashed lines: constraint boundaries; shaded: Q or Q^+ .

Multi-MNIST — HyperTrans Model

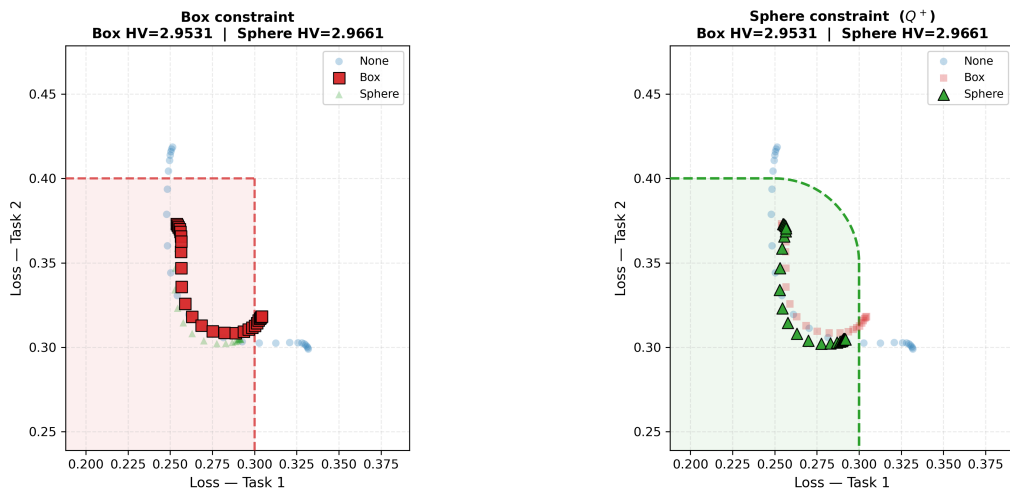


Figure 12: Multi-MNIST, ABP-HyperTrans: layout as in Fig. 11.

Multi-Fashion — Hyper-MLP Model

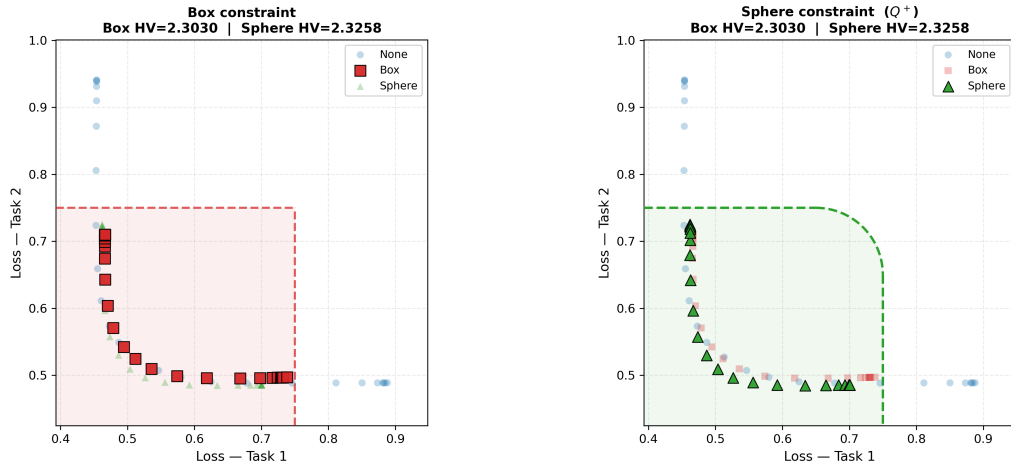


Figure 13: Multi-Fashion, ABP-HyperMLP: layout as in Fig. 11.

Multi-Fashion — HyperTrans Model

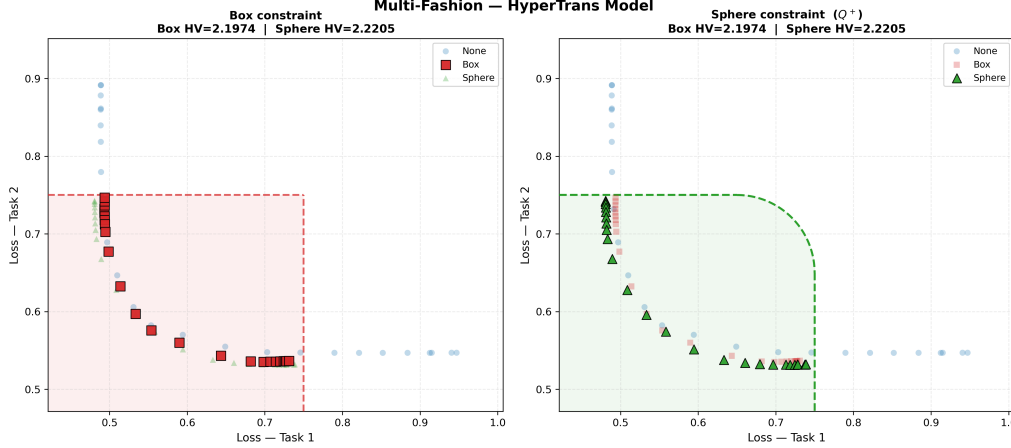


Figure 14: Multi-Fashion, ABP-HyperTrans: layout as in Fig. 11.

Fashion+MNIST — Hyper-MLP Model

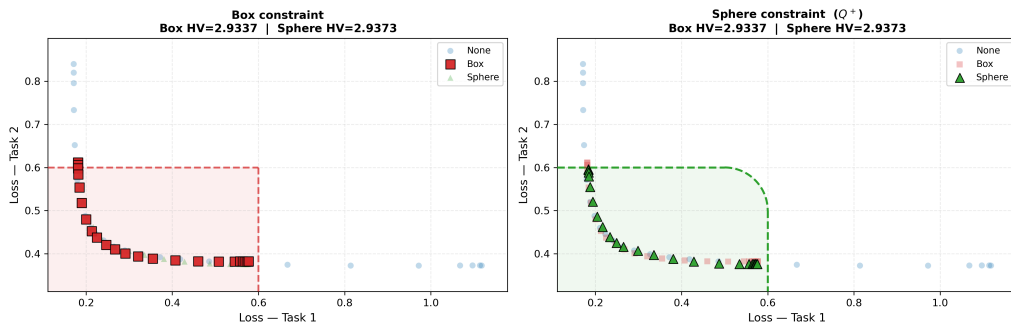


Figure 15: Fashion+MNIST, ABP-HyperMLP: layout as in Fig. 11.

Fashion+MNIST — HyperTrans Model

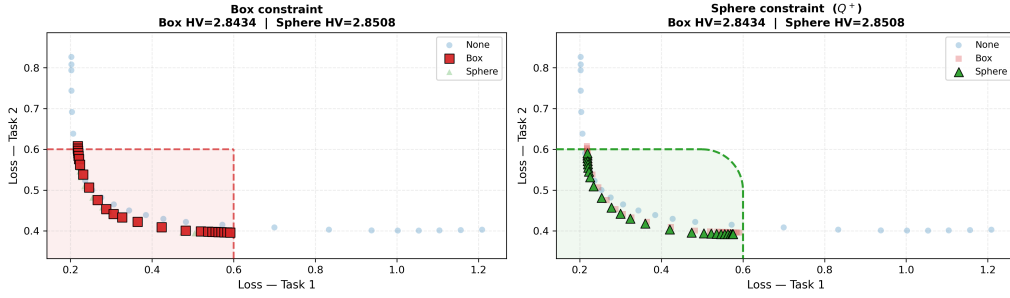


Figure 16: Fashion+MNIST, ABP-HyperTrans: layout as in Fig. 11.

HyperTransformer Predictions over Unconstrained PF

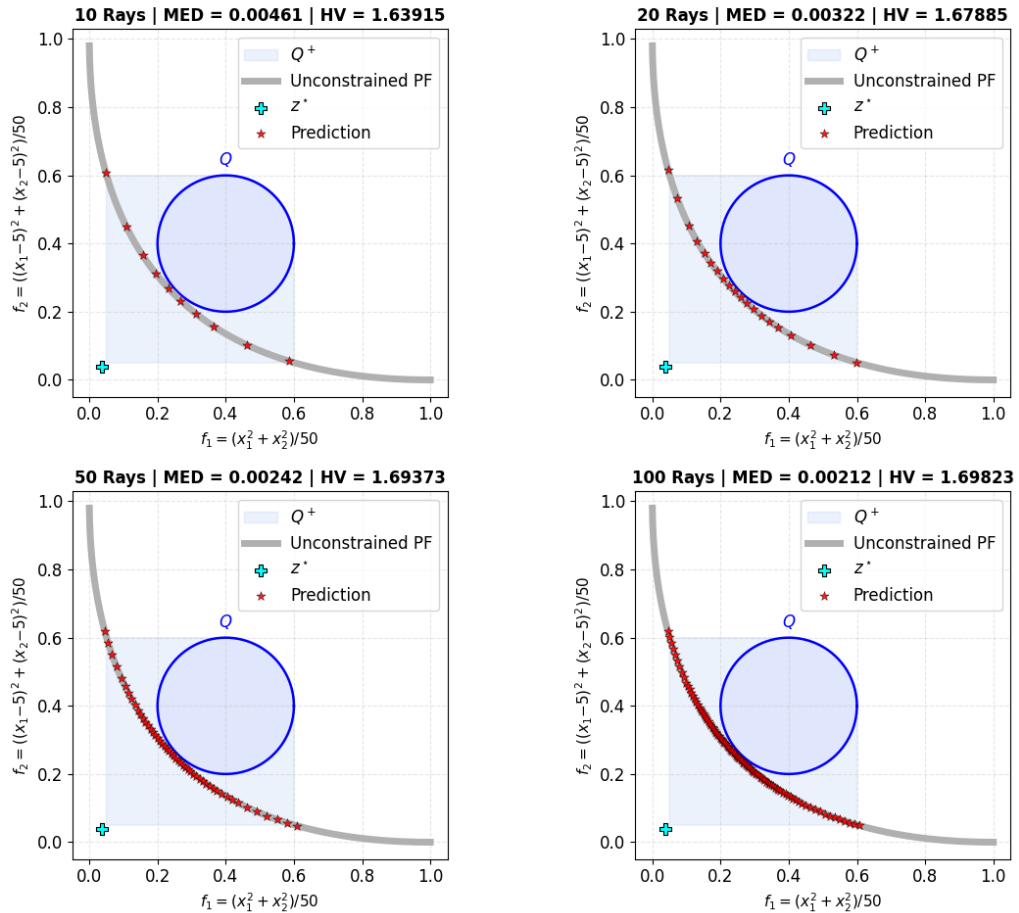


Figure 17: ABP-HyperTrans predictions on CVX2 at 10, 20, 50, and 100 preference rays. Grey curve: unconstrained Pareto front; blue circle: boundary of Q ; shaded region: Q^+ ; red stars: predicted solutions; cyan cross: z^* .

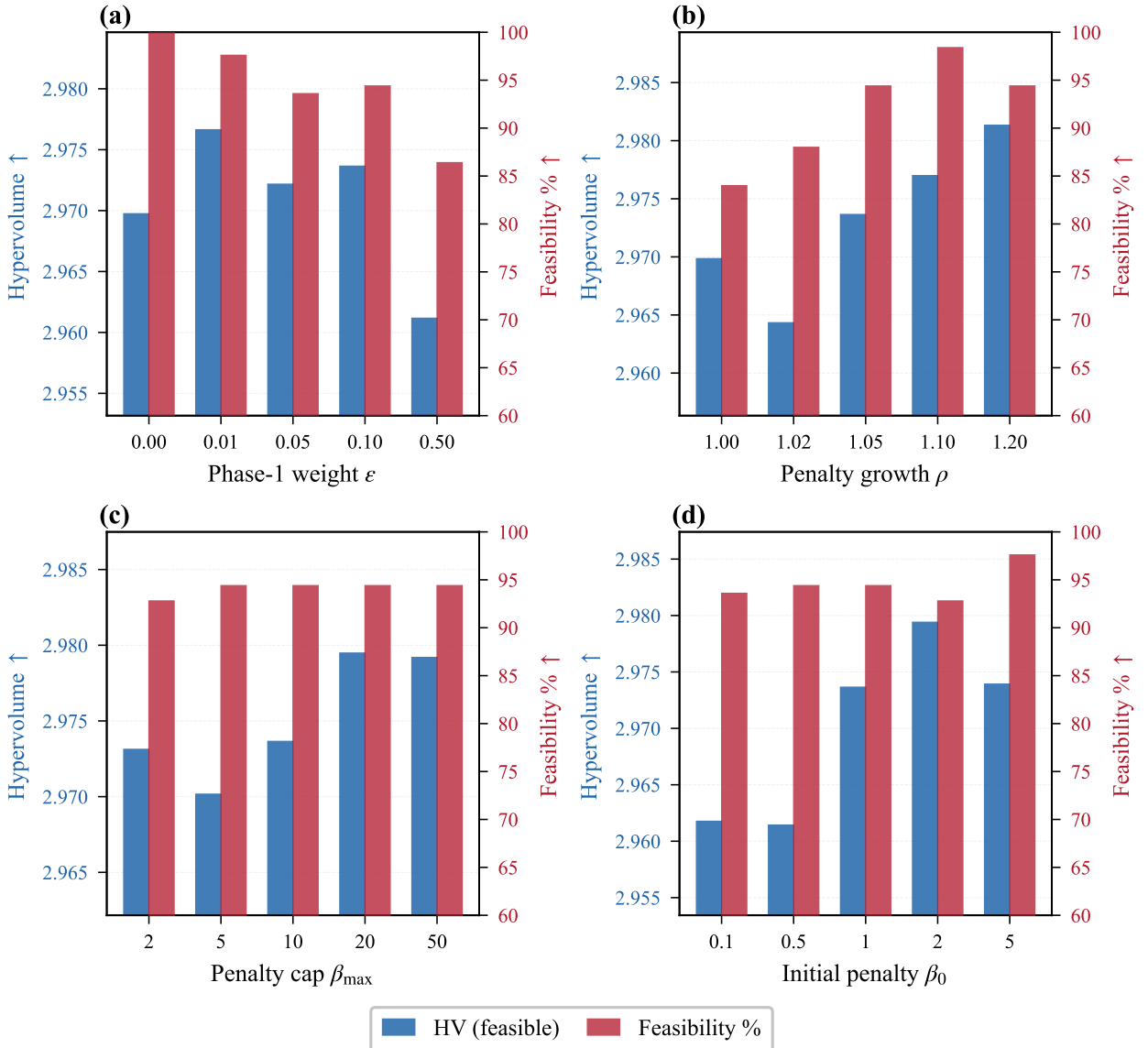


Figure 18: Hyperparameter sensitivity on Multi-MNIST (Hyper-MLP, Box constraint) across four key parameters. Bars represent the mean over 5 independent seeds for (a) Phase-1 weight ϵ , (b) penalty growth ρ , (c) penalty cap β_{\max} , and (d) initial penalty β_0 .

CRedit authorship contribution statement

Nguyen Viet Hoang: Methodology, Software, Validation, Writing – Original Draft. **Dung D. Le:** Supervision, Writing – Review & Editing. **Tran Ngoc Thang:** Methodology, Conceptualization, Formal Analysis, Supervision, Writing – Review & Editing.

Declaration of competing interest

The authors declare that they have no known competing financial interests or personal relationships that could have appeared to influence the work reported in this paper.

Data availability

The Multi-MNIST, Multi-Fashion, and Fashion+MNIST benchmark datasets used in this study are publicly available at https://github.com/longhp1618/MultiSample-Hypernetworks/tree/main/Multi_MNIST/data. The MOP benchmark problems (CVX1–3, ZDT1–2) are fully specified by the analytical definitions in Section 6.1 and require no additional data files. Source code for reproducing the experiments will be made publicly available in a dedicated repository upon acceptance of the manuscript.

References

- Achiam, J., Held, D., Tamar, A., Abbeel, P., 2017. Constrained policy optimization, in: International Conference on Machine Learning (ICML), pp. 22–31.
- Agarwal, A., Beygelzimer, A., Dudík, M., Langford, J., Wallach, H., 2018. A reductions approach to fair classification, in: International Conference on Machine Learning (ICML), pp. 60–69.
- Altman, E., 1999. Constrained Markov decision processes. Chapman & Hall/CRC, Boca Raton, FL.
- Bauschke, H.H., Combettes, P.L., 2017. Convex analysis and monotone operator theory in Hilbert spaces. 2nd ed., Springer, Cham.
- Bertsekas, D.P., 1999. Nonlinear programming. 2nd ed., Athena Scientific, Belmont, MA.
- Binh, T.T., Korn, U., 1997. Mobes: A multiobjective evolution strategy for constrained optimization problems, in: The third international conference on genetic algorithms (Mendel 97), p. 27.
- Brooke, M., Censor, Y., Gibali, A., 2021. Dynamic string-averaging cq-methods for the split feasibility problem with percentage violation constraints arising in radiation therapy treatment planning. International Transactions in Operational Research 30, 181–205
- Byrne, C., 2002. Iterative oblique projection onto convex sets and the split feasibility problem. Inverse problems 18, 441
- Byrne, C., 2004. A unified treatment of some iterative algorithms in signal processing and image reconstruction. Inverse Problems 20, 103–120.
- Cao, X., Jia, S., Luo, Y., Yuan, X., Qi, Z., Yu, K.T., 2019. Multi-objective optimization method for enhancing chemical reaction process. Chemical Engineering Science 195, 494–506.
- Censor, Y., Elfving, T., 1994. A multiprojection algorithm using bregman projections in a product space. Numerical Algorithms 8, 221–239.
- Censor, Y., Elfving, T., Kopf, N., Bortfeld, T., 2005. The multiple-sets split feasibility problem and its applications for inverse problems. Inverse problems 21, 2071.
- Censor, Y., Gibali, A., Reich, S., 2012. Algorithms for the split variational inequality problem. Numerical Algorithms 59, 301–323.
- Ehrgott, M., 2005. Multicriteria optimization. volume 491. Springer Science & Business Media.
- Emmerich, M.T.M., Giannakoglou, K.C., Naujoks, B., 2006. Single- and multiobjective evolutionary optimization assisted by Gaussian random field metamodels. IEEE Transactions on Evolutionary Computation 10, 421–439.
- Gelbart, M.A., Snoek, J., Adams, R.P., 2014. Bayesian optimization with unknown constraints, in: Proceedings of the 30th Conference on Uncertainty in Artificial Intelligence (UAI), pp. 250–259.
- Hiriart-Urruty, J.-B., Lemaréchal, C., 2004. Fundamentals of convex analysis. Springer, Berlin.
- Jangir, P., Heidari, A.A., Chen, H., 2021. Elitist non-dominated sorting harris hawks optimization: Framework and developments for multi-objective problems. Expert Systems with Applications 186, 115747.
- Kim, N.T.B., Thang, T.N., 2013. Optimization over the efficient set of a bicriteria convex programming problem. Pac. J. Optim. 9, 103–115.
- Lan, G., Monteiro, R.D.C., 2013. Iteration-complexity of first-order penalty methods for convex programming. Mathematical Programming 138, 115–139.
- Lin, X., Zhen, H.L., Li, Z., Zhang, Q., Kwong, S., 2019. Pareto multi-task learning, in: Thirty-third Conference on Neural Information Processing Systems (NeurIPS), pp. 12037–12047.
- Lin, X., Yang, Z., Zhang, Q., 2022. Pareto set learning for expensive multi-objective optimization. Advances in Neural Information Processing Systems 35, 16298–16310.
- Miettinen, K., 1999. Nonlinear multiobjective optimization. Kluwer Academic Publishers, Boston.
- Navon, A., Shamsian, A., Chechik, G., Fetaya, E., 2021. Learning the Pareto front with hypernetworks, in: International Conference on Learning Representations (ICLR).
- Nesterov, Y., 2004. Introductory lectures on convex optimization: a basic course. Kluwer Academic Publishers, Boston.
- Raissi, M., Perdikaris, P., Karniadakis, G.E., 2019. Physics-informed neural networks: A deep learning framework for solving forward and inverse problems involving nonlinear partial differential equations. Journal of Computational Physics 378, 686–707.

- Robbins, H., Monro, S., 1951. A stochastic approximation method. *Annals of Mathematical Statistics* 22, 400–407.
- Robbins, H., Siegmund, D., 1971. A convergence theorem for non-negative almost supermartingales and some applications, in: Rustagi, J.S. (Ed.), *Optimizing methods in statistics*. Academic Press, New York, pp. 233–257.
- Rockafellar, R.T., Wets, R.J.-B., 2009. *Variational analysis*. Springer, Berlin.
- Rockafellar, R.T., 1970. *Convex analysis*. Princeton University Press, Princeton, NJ.
- Sabour, S., Frosst, N., Hinton, G.E., 2017. Dynamic routing between capsules, in: *Advances in Neural Information Processing Systems (NeurIPS)*, pp. 3859–3869.
- Sener, O., Koltun, V., 2018. Multi-task learning as multi-objective optimization. *Advances in neural information processing systems* 31.
- Thang, T.N., Solanki, V.K., Dao, T.A., Thi Ngoc Anh, N., Van Hai, P., 2020. A monotonic optimization approach for solving strictly quasiconvex multiobjective programming problems. *Journal of Intelligent & Fuzzy Systems* 38, 6053–6063.
- Tuan, T.A., Hoang, L.P., Le, D.D., Thang, T.N., 2024. A framework for controllable Pareto front learning with completed scalarization functions and its applications. *Neural Networks* 169, 257–273.
- Tuan, T.A., Dung, N.V., Thang, T.N., 2024. A HyperTrans model for controllable Pareto front learning with split feasibility constraints. *Neural Networks* 179, 106571.
- Vuong, N.D., Thang, T.N., 2023. Optimizing over pareto set of semistrictly quasiconcave vector maximization and application to stochastic portfolio selection. *Journal of Industrial and Management Optimization* 19, 1999–2019.
- Xiao, H., Rasul, K., Vollgraf, R., 2017. Fashion-MNIST: a novel image dataset for benchmarking machine learning algorithms. *arXiv preprint arXiv:1708.07747*.
- Yun, C., Bhojanapalli, S., Rawat, A.S., Reddi, S.J., Kumar, S., 2020. Are transformers universal approximators of sequence-to-sequence functions?, in: *International Conference on Learning Representations (ICLR)*.
- Zitzler, E., Thiele, L., 1999. Multiobjective evolutionary algorithms: a comparative case study and the strength pareto approach. *IEEE transactions on Evolutionary Computation* 3, 257–271.
- Zitzler, E., Deb, K., Thiele, L., 2000. Comparison of multiobjective evolutionary algorithms: Empirical results. *Evolutionary computation* 8, 173–195.

Declaration of Generative AI and AI-assisted technologies in the writing process

During the preparation of this work the authors used Claude (Anthropic) for language editing and improving readability. After using this tool, the authors reviewed and edited the content as needed and take full responsibility for the content of the publication.